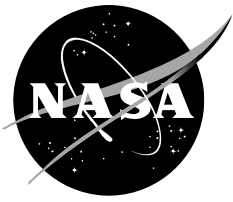


NASA/TP—2012–216315



Two Dimensional Heat Transfer around Penetrations in Multilayer Insulation Final Report

*Wesley L. Johnson and Andrew O. Kelly
Fluids Test and Technology Development Branch
Kennedy Space Center, Florida*

*Kevin M. Jumper
Sierra Lobo, Kennedy Space Center, FL*

October 2012

NASA STI Program ... in Profile

Since its founding, NASA has been dedicated to the advancement of aeronautics and space science. The NASA scientific and technical information (STI) program plays a key part in helping NASA maintain this important role.

The NASA STI program operates under the auspices of the Agency Chief Information Officer. It collects, organizes, provides for archiving, and disseminates NASA's STI. The NASA STI program provides access to the NASA Aeronautics and Space Database and its public interface, the NASA Technical Reports Server, thus providing one of the largest collections of aeronautical and space science STI in the world. Results are published in both non-NASA channels and by NASA in the NASA STI Report Series, which includes the following report types:

- **TECHNICAL PUBLICATION.** Reports of completed research or a major significant phase of research that present the results of NASA Programs and include extensive data or theoretical analysis. Includes compilations of significant scientific and technical data and information deemed to be of continuing reference value. NASA counterpart of peer-reviewed formal professional papers but has less stringent limitations on manuscript length and extent of graphic presentations.
- **TECHNICAL MEMORANDUM.** Scientific and technical findings that are preliminary or of specialized interest, e.g., quick release reports, working papers, and bibliographies that contain minimal annotation. Does not contain extensive analysis.
- **CONTRACTOR REPORT.** Scientific and technical findings by NASA-sponsored contractors and grantees.

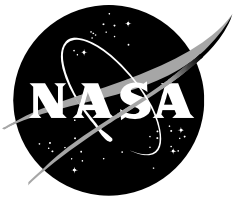
- **CONFERENCE PUBLICATION.** Collected papers from scientific and technical conferences, symposia, seminars, or other meetings sponsored or co-sponsored by NASA.
- **SPECIAL PUBLICATION.** Scientific, technical, or historical information from NASA programs, projects, and missions, often concerned with subjects having substantial public interest.
- **TECHNICAL TRANSLATION.** English-language translations of foreign scientific and technical material pertinent to NASA's mission.

Specialized services also include organizing and publishing research results, distributing specialized research announcements and feeds, providing information desk and personal search support, and enabling data exchange services.

For more information about the NASA STI program, see the following:

- Access the NASA STI program home page at <http://www.sti.nasa.gov>
- E-mail your question to help@sti.nasa.gov
- Fax your question to the NASA STI Information Desk at 443-757-5803
- Phone the NASA STI Information Desk at 443-757-5802
- Write to:
STI Information Desk
NASA Center for Aerospace Information
7115 Standard Drive
Hanover, MD 21076-1320

NASA/TP—2012–216315



Two Dimensional Heat Transfer around Penetrations in Multilayer Insulation Final Report

*Wesley L. Johnson and Andrew O. Kelly
Fluids Test and Technology Development Branch
Kennedy Space Center, Florida*

*Kevin M. Jumper
Sierra Lobo, Kennedy Space Center, FL*

National Aeronautics and
Space Administration

*Kennedy Space Center
Kennedy Space Center, FL 32899-0001*

October 2012

Acknowledgments

The authors would like to acknowledge Wayne Heckle and Johnny Kerce for performing a majority of the testing in this report and James Fesmire for his support and guidance in boil-off calorimetry.

Available from:

NASA Center for AeroSpace Information
7115 Standard Drive
Hanover, MD 21076-1320
443-757-5802

National Technical Information Service
5301 Shawnee Road
Alexandria, VA 22312
703-605-6000

This report is also available in electronic form at [http:// www.sti.nasa.gov](http://www.sti.nasa.gov)

Table of Contents

1	Background.....	4
2	Introduction.....	6
3	Experimental.....	8
3.1	Instrumentation.....	10
3.2	MLI Blankets.....	13
3.3	Penetrations.....	15
3.4	Buffer Materials.....	18
3.5	Test Matrix.....	19
3.6	Experimental Uncertainty.....	21
3.7	System Data.....	22
4	Thermal Models.....	26
4.1	Model Overview.....	26
4.1.1	Cryostat Detailed Model Overview.....	26
4.1.2	Scaling Model Overview.....	28
4.1.3	Cryostat Detailed Model Validation.....	29
4.1.4	Detailed Model Validation Discussion.....	33
4.1.5	Scaling Model Results.....	34
5	Test Results and Analysis.....	39
5.1	No Penetration – Null testing.....	40
5.2	No Integration.....	42
5.3	Buffer Materials.....	42
5.4	Temperature Matching.....	47
6	Conclusion.....	50
	References.....	52
	Appendix A – More data plots.....	53
	Appendix B – Sample Calculation.....	58
	Appendix C – Uncertainty Analysis Derivations.....	60

List of Figures

Figure 1: Schematic of Insulation Penetration Cryostat, Reference 1: Figure 18.....	4
Figure 2: Installation of fiberglass strut, Reference 2: Figure 6.	5
Figure 3: Shield-penetration grid and shield-buffer-penetration grid, Reference 3: Figures 2a and 3a.....	5
Figure 4: Cryostat-600 cold mass during liquid nitrogen cold shock	8
Figure 5: Passive heater attached to the half inch diameter strut	9
Figure 6: Schematic & controls diagram for Cryostat-600	10
Figure 7: Temperature sensor locations with no strut.....	12
Figure 8: Temperature sensor location with strut present (assumes a 0.5" thick buffer).....	13
Figure 9: Thermocouples in a semi-circular pattern	14
Figure 10: Punch used to insert holes into MLI blankets.....	14
Figure 11: G-10 MLI support shown holding up MLI underneath Cryostat-600	15
Figure 12: Threaded taps on the bottom of Cryostat-600	16
Figure 13: Composite strut for penetration testing.	17
Figure 14: Aerogel bead package.....	19
Figure 15: General Test Matrix for Penetrations Calorimetry	20
Figure 16: Temperature profile of MLI and penetrations through the thickness of the MLI.....	21
Figure 17: Typical mass flow rates and fill level data	23
Figure 18: Typical system temperatures and preferences	24
Figure 19: Typical MLI temperatures	25
Figure 20: Steady state MLI temperatures plotted vs. location	25
Figure 21: Section View of Detailed Model	28
Figure 22: Predicted Temperature Across Cold Mass.....	33
Figure 23: Change in Heat Leak with Penetration Diameter	35
Figure 24: Change in Heat Leak with Buffer Thickness.....	37
Figure 25: Change in Heat Leak with number of MLI layers.....	38
Figure 26: Test Result Summary for Penetration Calorimetry	39
Figure 27: Temperature Profile for P100	41
Figure 28: Temperature Profile for P118	41
Figure 29: Temperature profiles for No Integration testing on Aluminum strut	42
Figure 30: Aerogel blanket buffer - 0.5" (0.25" radius).....	43
Figure 31: Aerogel beads packed in nylon and installed on calorimeter	44
Figure 32: 1" (0.5" radius) Cryo-Lite buffer.....	44
Figure 33: P115, 1 inch buffer, 0.25" strut 2-D thermal projection	45
Figure 34: Composite strut installed on calorimeter with a Cryo-Lite buffer.....	47
Figure 35: Predicted MLI and penetration temperature gradients	48
Figure 36: Temperature gradients through MLI showing predicted, P100, and P112. Also shown for reference are the strut temperatures.	49
Figure 37: Comparison between different integration methods for a half inch aluminum penetration	50

List of Tables

Table 1: Key Performance Parameters for Penetrations Testing	7
Table 2: Pressure transducers and their ranges	11
Table 3: Description of the four struts tested.....	17
Table 4: Buffer material descriptions.....	19
Table 5: Uncertainty Analysis Results.....	22
Table 6: Material properties used in the calorimeter thermal model	26
Table 7: Typical Cold Mass Temperatures	27
Table 8: Penetration Heat Load Predicted From Model Compared With Test Result Calculations.....	30
Table 9: Penetration Heat Load - Test vs Model	32
Table 10: Test P115 Strut Temperature Data.....	32
Table 11: No penetration MLI test results	40
Table 12: Results from buffer material testing at different buffer thicknesses	43
Table 13: Test Results for Cryo-Lite Buffers on various penetration sizes	46
Table 14: Temperature matching locations along the strut (total length .203 m)	48

1 Background

Cryogenic multilayer insulation (MLI) has been studied thoroughly over the last 50 years. Numerous tank and calorimeter tests have been performed using many different insulation approaches. Many different variables have been tested and documented, mainly within the insulation system itself. There are several factors in insulation application that can drive up the heat load on the entire system. These include the treatment of insulation seams, instrumentation wires running through the insulation, and the integration of the insulation with the structural and fluids.

Several attempts have been made to identify the performance losses due to structural integration with a real system. (1-3) In Reference 1, Coston, Murray, and Lambert investigated the losses due to penetrations using the device shown in Figure 1. They investigated using an intermediary buffer made of Dexiglass (which at the time was often used as the spacer in MLI) of three and five inches. In cooperation with thermal models, the heat load was found to minimize at a point much less than the three inches thick buffer. They could not measure a meaningful added heat load through the insulation except for in the five inch thick Dexiglass buffer. In Reference 2, Sumner installed a fiberglass strut onto a liquid hydrogen calorimeter as shown in Figure 2. No buffer or intermediary was installed around the strut and the degradation area was half of a meter with an excess heat load of just over 0.4 W due to the integration. In Reference 3, Johnson and Sprague built a nodal based thermal model which they used to explore the relationship between the strut, MLI, and a buffer (see Figure 3). They used aluminum foil for the reflection layers and a general isotropic material with thermal conductivity of 16 mW/m-K as a buffer material. The end result of their modeling provided equations for estimating the net excess heat load into the tank as well as the degradation area of the MLI for each configuration.

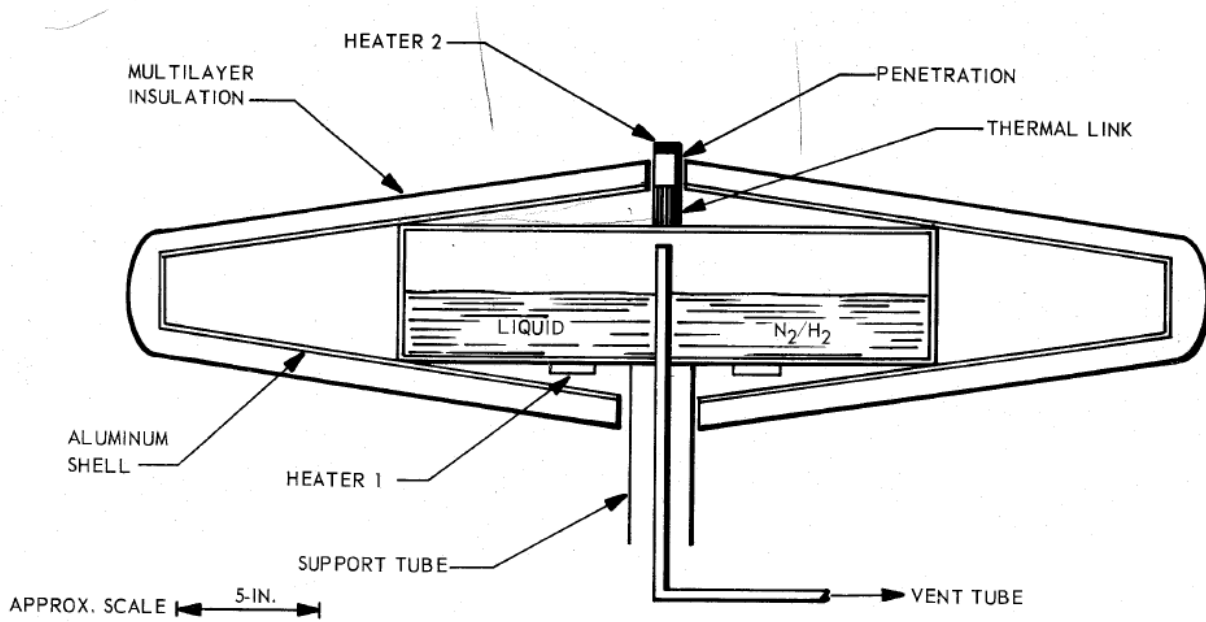


Figure 1: Schematic of Insulation Penetration Cryostat, Reference 1: Figure 18

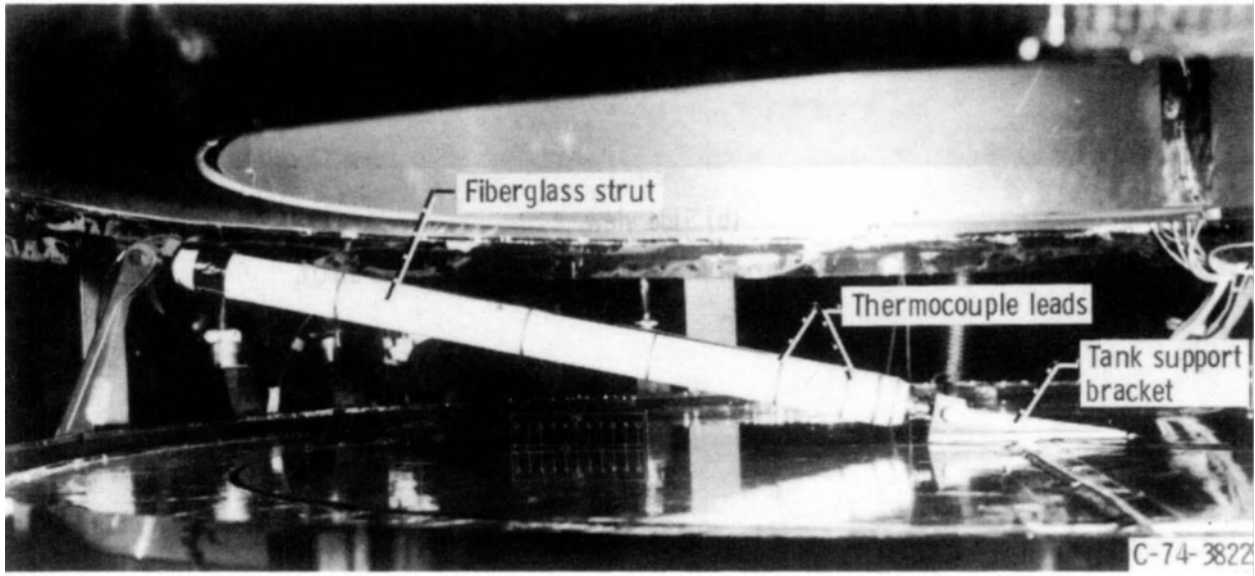


Figure 2: Installation of fiberglass strut, Reference 2: Figure 6.

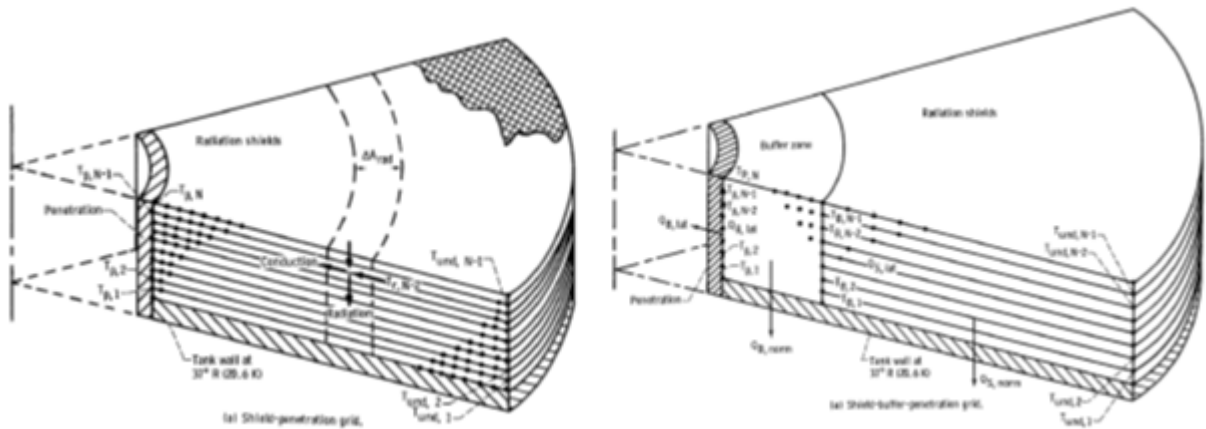


Figure 3: Shield-penetration grid and shield-buffer-penetration grid, Reference 3: Figures 2a and 3a.

Due to the nature of MLI, these were tied to specific programs and configuration dependent. In a review of the state of the art for multilayer insulation applications, it was determined that uncertainty related to the integration of penetrations through the MLI was a risk to demonstrating a high performance system in low earth orbit.

2 Introduction

The objective of this task was to quantify thermal losses involving integrating MLI into real life situations. Testing specifically focused on the effects of penetrations (including structural attachments, electrical conduit/feedthroughs, and fluid lines) through MLI. While there have been attempts at quantifying these losses both analytically and experimentally, none have included a thorough investigation of the methods and materials that could be used in such applications.

To attempt to quantify the excess heat load coming into the system due to the integration losses, a calorimeter was designed to study two dimensional heat transfer through penetrated MLI. The test matrix was designed to take as many variables into account as was possible with the limited test duration and system size. The parameters varied were the attachment mechanism, the buffer material (for buffer attachment mechanisms only), the thickness of the buffer, and the penetration material.

The work done under this task is an attempt to measure the parasitic heat loads and affected insulation areas produced by system integration, to model the parasitic loads, and from the model produce engineering equations to allow for the determination of parasitic heat loads in future applications. The methods of integration investigated were no integration, using a buffer to thermally isolate the strut from the MLI, and temperature matching the MLI on the strut. Several materials were investigated as a buffer material including aerogel blankets, aerogel bead packages, cryolite, and even an evacuated vacuum space (in essence a no buffer condition).

A very specific method was used to quantify the integration dependent heat loads. First the MLI blanket was tested with no penetrations to provide a baseline heat load case. The test penetrations were made out of known materials, either aluminum or carbon fiber composites, with known geometries to allow for the heat load down the penetration to be easily calculated using Fourier's Law and two temperatures measured along the penetration:

$$Q_{Pen} = \frac{k A (\Delta T)}{x}$$

The parasitic integration heat load could then be calculated by subtracting the MLI and penetration heat loads from the measured heat loads. Ideally, if there were no integration losses, this would be zero.

$$\Delta Q_{Integ} = Q_{meas} - Q_{MLI} - Q_{Pen}$$

To measure the affected insulation zone, temperature sensors were placed within the MLI blanket on layers 3, 8, 16, and 25 at predetermined spacing. Thus by starting at the center of the blanket and working out radially, temperature gradients could be determined and if they were within the uncertainty of the thermocouple (roughly 1 K), then it was assumed that the affected area had ended. All degradation radii are measured from the center of the penetration and are determined to be where the temperature changed by 1 K or less.

The Key Performance Parameters for the testing are shown in Table 1.

Table 1: Key Performance Parameters for Penetrations Testing

KPP	Minimum Success	Full Success
Integration Heat Load (W)	< 0.2	< 0.1
Temperature affected zone (m)	0.05	0.02

Two different types of thermal models have been developed for the system. The first is a Thermal Desktop model, where the whole calorimeter system was modeled. The actual materials used in building the calorimeter along with their appropriate mechanical, thermal, and optical properties were input into the Thermal Desktop model. The Thermal Desktop model was used to better understand the testing and how to interpret the testing. Additionally, once validated with test data, the model was scaled to allow for extrapolation on several parameters.

3 Experimental

To perform the desired testing, a guarded flat plate calorimeter was designed and fabricated for this special application. The outer diameter of the guard chamber is 12.000 inches and the height is 7.50 inches. The test chamber is 8.230 inches in diameter and 2.50 inches tall. Four threaded taps were put into the bottom surface of the calorimeter to allow for the attachment of the various penetrations. Both the test and guard chambers were leak checked to 1×10^{-8} sccs following cold shock with liquid nitrogen (see Figure 4).



Figure 4: Cryostat-600 cold mass during liquid nitrogen cold shock

After cold shock, the cold mass instrumentation was then placed on the vessel to measure the temperature on the bottom of the cold mass, on the side a few inches from the top and on the top of the cold mass. A half inch versify strip was attached to the cold mass to provide an edge guard for the test samples. Then the top and sides of the guard chamber were wrapped with 10 layers of multilayer insulation.

Heaters were wrapped around the vacuum chamber and installed on the outer surface of a cylinder made from aluminum sheet which was placed inside of the vacuum chamber. The inside of the cylinder was painted with Aeroglaze Z306 Flat Black Absorptive Polyurethane (4) to provide a black environment to simulate space and to allow for baking out of samples prior to testing. In addition to heaters internal and external to the vacuum chamber, a “passive heater” was hung on the end of the penetration to maintain the warm boundary on the end of the penetration and extend the absorptive view to the bottom of the test area (see Figure 5). The passive heater was also painted with the Aeroglaze Z306. Using an A-Z Technology TESA

2000 reflectometer, the solar absorptivity of the Aeroglaze Z306 was measured at 0.945 and the infrared emissivity was measured at 0.89.

At the beginning of each test, the back pressure control system that is connected to both Cryostat-100 and Cryostat-600 was set to control the pressure at 3 Torr above the current local ambient pressure at ± 0.1 Torr. This helped to dampen oscillations in the liquid nitrogen heat of vaporization due to changes in local atmospheric pressure. During testing, the guard and test chambers are periodically topped off to ensure that neither one runs out of fluid.



Figure 5: Passive heater attached to the half inch diameter strut

3.1 Instrumentation

Instrumentation on Cryostat-600 includes temperature sensors, pressure transducers, and flow meters. The pressure transducers and flow meters are shown in the schematic below (see Figure 6). MKS 10MB series of mass flow meters were used for all testing. These flow meters use thermal anemometry to measure the mass flow rate of the gas through an orifice. The Cryogenics Test Laboratory has approximately 40 flow meters, all of which are calibrated using in-house NASA standards and are accurate to +/- 2% or less over the range of the flow meter.

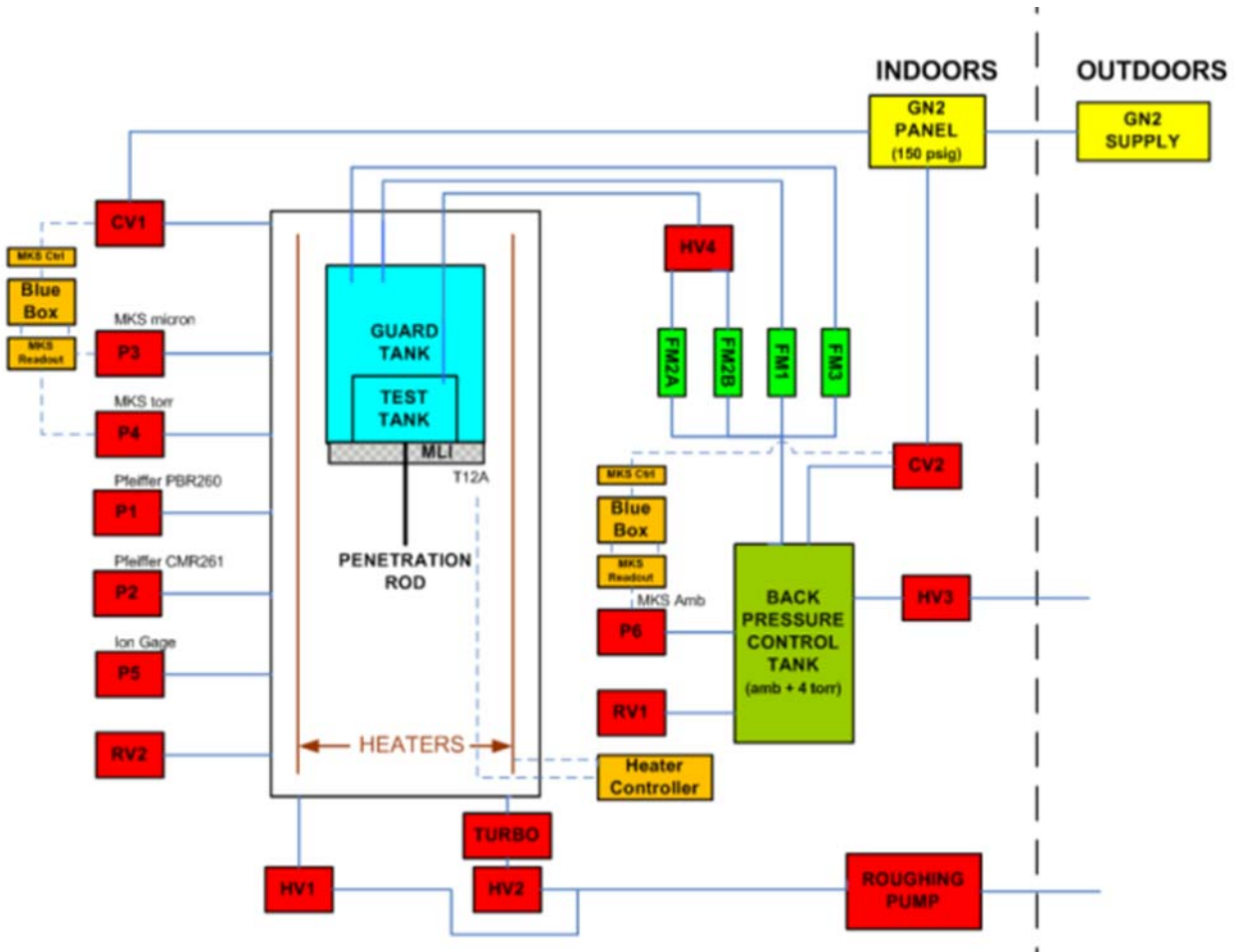


Figure 6: Schematic & controls diagram for Cryostat-600

The pressure transducers cover the whole range of vacuum pressure between atmospheric pressure and 1×10^{-7} Torr. Additionally, a pressure transducer is placed on the back pressure control system to allow for control of the system. The pressure control systems consist of the MKS Baratron capacitance manometers (and readout), a switching box to pick a signal from the readout to send to the control module, and a MKS 250E pressure/flow control module that regulates an MKS 248A flow control valve. The desired pressure setting (by means of voltage) is set on the user panel of the MKS 250E control module, which contains proportional, integral, and derivate based control logic. The details for each pressure transducer are shown in Table 2. During checkout testing, the Granville-Phillips Micro-Ion gauge was not turned off when the vacuum chamber was repressurized. This caused the gauge to overheat and fail. The remainder of the testing was done with the Pfeiffer PBR 260 gauge substituting for the Micro-Ion gauge below 1×10^{-5} torr.

To measure the temperatures within the test apparatus, 21 type-E 36 gauge thermocouples were attached in various locations. Prior to installation, the thermocouples were submersed in a liquid nitrogen bath and then an ice water bath and matched within a few tenths of a Kelvin.

Three of the thermocouples were on the cold mass: one on the top of the guard (T1), one on the side of the guard chamber approximately 12.7mm from the top (T2), and one on the bottom of the test chamber (T3), roughly one inch from the center (off center due to strut presence). Five thermocouples were reserved for the penetration (T4-7, 13). Two thermocouples were reserved for the heater (T12) and heater controller (T12H). The remaining 15 thermocouples were interspersed within the MLI on layers 3, 8, 16, and 25. Figure 7 and Figure 8 show the temperature sensor placement within the MLI blanket for the no-penetration and penetration cases. As the penetration and buffer grew larger, the displaced thermocouples were generally set to the edge of the hole in the MLI and then 10 mm outside of that thermocouple.

Table 2: Pressure transducers and their ranges

Instrument Tag	Description	Range
P1	Pfeiffer PBR 260	$10^{-10} - 10^3$ Torr
P2	Pfeiffer CMR 361	$10^{-2} - 10^3$ Torr
P3	MKS Baratron capacitance manometer	$10^{-4} - 10^{-1}$ Torr
P4	MKS Baratron capacitance manometer	0.1 – 100 Torr
P5	Granville-Phillips Micro-Ion gauge	$10^{-9} - 10^{-2}$ Torr
P6	MKS Baratron capacitance manometer	1 – 1000 Torr

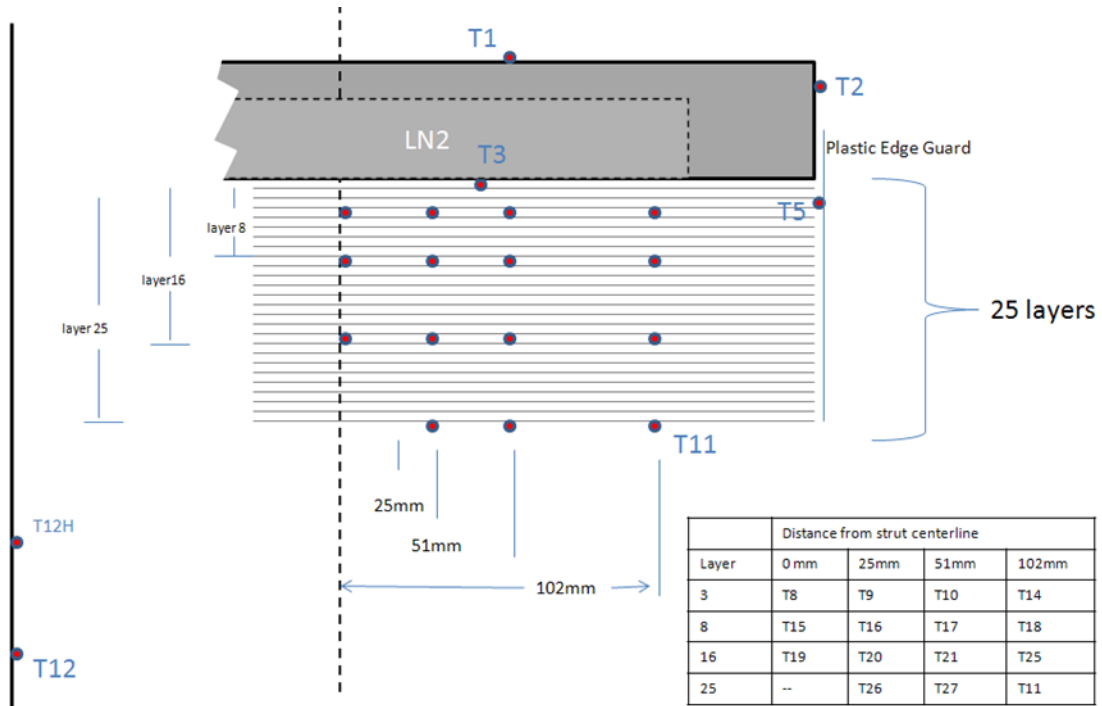


Figure 7: Temperature sensor locations with no strut

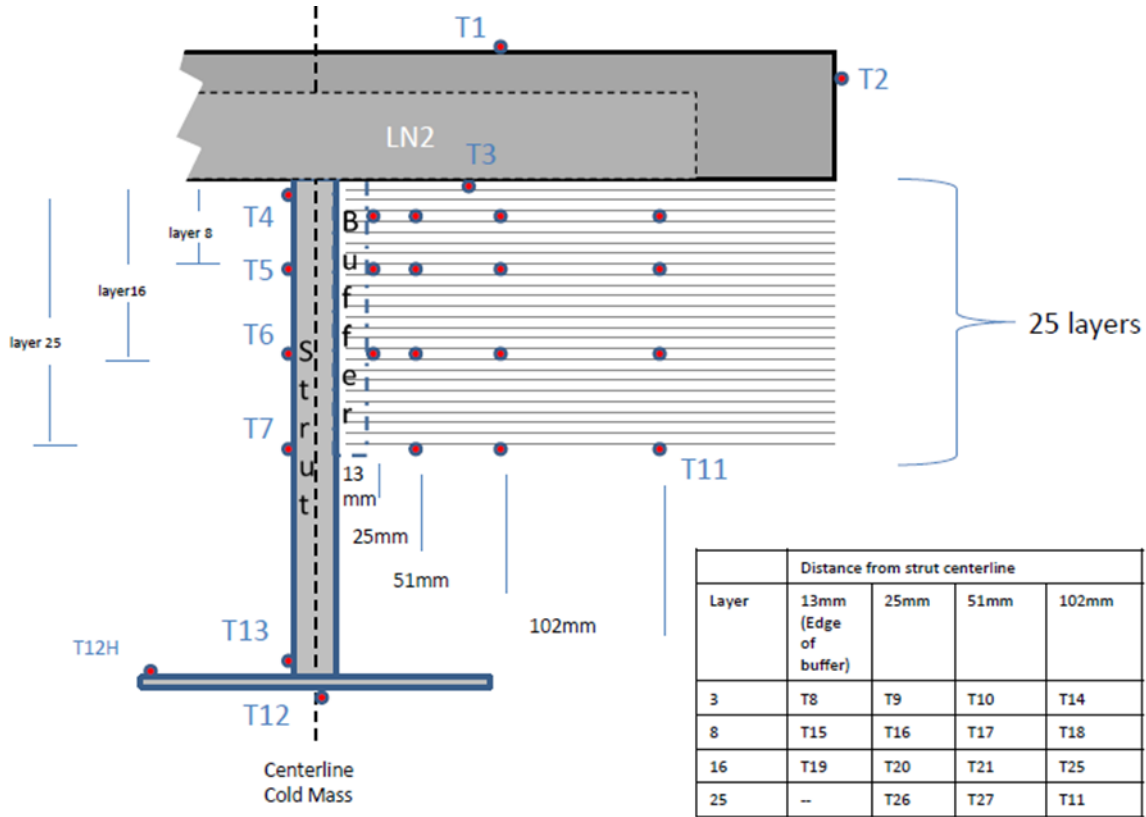


Figure 8: Temperature sensor location with strut present (assumes a 0.5" thick buffer)

3.2 MLI Blankets

A total of 8 MLI blankets were cut out for testing. The first four were cut on August 15, 2011 and the second four were cut out on September 30, 2011. All the blankets were 25 layers (with one layer consists of both a reflector and spacer material). The reflector material is Dunmore DE 028 dated from 9/09 (0.25 mil unperforated double aluminized mylar). The emissivity of the mylar was measured to be less than 0.03. The spacer material is Dacron B4A netting acquired from Aerospace Fabrication and Materials.

All thermocouples were routed in a semi-circular pattern around the MLI blanket as shown in Figure 9. This lengthened the thermocouple leads considerable and lowered the thermal conductance of those leads into the blanket. Overall, the thermocouples added on the order of 5 mW to the total heat load of the blanket, well under the uncertainty of the entire system.



Figure 9: Thermocouples in a semi-circular pattern

In order to put the penetration through the MLI, holes were punched in the MLI. A standard tooling punch (see Figure 10) was used that has punches from 1/8th of an inch all the way to 2" at approximately 1/16th intervals. Generally, the punched hole was sized to be 1/16th inch larger on the diameter than the strut plus the buffer size. From best practices, thermocouples were always moved prior to punching the hole and replaced if necessary after the hole was punched. This prevented the accidental destruction of a thermocouple bead.



Figure 10: Punch used to insert holes into MLI blankets

A G-10 ring with Kevlar string cross thread was used to hold the MLI into place underneath the cold mass (see Figure 11). The G-10 ring was held in place one half of an inch below the cold mass with help from the Versify edge guard.

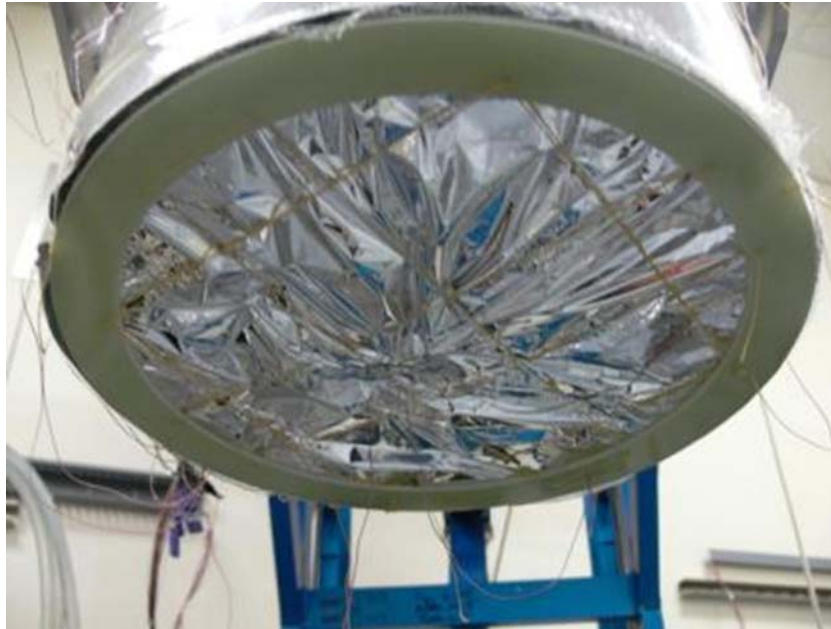


Figure 11: G-10 MLI support shown holding up MLI underneath Cryostat-600

3.3 Penetrations

Four different penetrations were built. Three were Aluminum 6061-T6 tubes (0.25" OD by 0.035" wall, 0.5" x 0.032", and 1.0" x 0.049") made from standard tubes with a welded end cap. The fourth was a composite strut made from two plies of carbon fiber tube (1.060" OD by 0.032" wall thickness) and Araldite LY8604/Aradur Epoxy Resin of which the fabrication process is further described below. An overview of the penetrations is given in Table 3. In order to minimize internal heat transfer, the tubes were filled with glass bubbles and capped with Lydall Cryo-Lite disks to prevent the bubbles from falling out. The tubes were attached to the calorimeter via threaded holes in the bottom of the calorimeter as shown in Figure 12. The ends of the penetrations were also lightly coated with Apeizon N type cryogenic thermal grease.

The Fesmire number is a number that relates the thermal and structural properties of a material. It is defined by the ratio of the compressive strength to the mass times the thermal conductance of the material. The Fesmire number for a material is defined as:

$$Fe = \frac{\sigma_{yield}}{\rho\lambda_t}$$

For a specific part or application, it can be specialized as:

$$Fe_s = \frac{F_{yield}}{mk_t}$$

Where:

Fe – Fesmire Number

Fe_s – Special Fesmire Number

m – mass (kg)

k_t – thermal conductance (W/m)

λ_t – thermal conductivity (W/m/K)

ρ – density (kg/m³)

σ_{yield} – tensile yield strength (MPa)

F_{yield} – force at which the part yields (kN)



Figure 12: Threaded taps on the bottom of Crysotat-600

Table 3: Description of the four struts tested

Strut Name	Strut Size (OD x wall thickness)	Strut Material	Strut Mass (g)	Buckling Load (kN)	Conductivity (W/K)	Special Fesmire Number
0.25" strut	0.25" x .035"	6061-T6 Aluminum	10.2	108	4.5e-3	2.4e6
0.5" strut	0.5" x 0.032"	6061-T6 Aluminum	27.1	89.3	2.2e-2	1.5e5
1" strut	1.0" x 0.049"	6061-T6 Aluminum	77.6	209	7.0e-2	3.9e4
Composite Strut	1.060" x 0.032"	Carbon sleeve/Araldite LY8604/Aradur Epoxy	20.4	10.4	7.5e-4	6.8e5



Figure 13: Composite strut for penetration testing.

The composite strut was made using braided carbon biaxial sleeve and the Araldite LY 8604/Aradur Epoxy Infusion System. A 1" round aluminum mandrel was prepared first by cleaning with Zyxax Fresh Start, treating the tool surface with Zyxax PreFlight, then applying the release agent Zyxax Departure to the tool surface. Two layers of carbon sleeve were then fitted and taped to the tool surface, one layer over the other. The carbon was then wrapped with a perforated release barrier with a layer of 1K 5 harness satin fiberglass on top of that as a bleeder material. On each end of the fiberglass bleeder a full wrap of spiral tubing was wound around the tool with each wrap of spiral tubing having its own flow tube attached. The tool was then bagged using a vacuum bagging film and sealant tape, allowing the flow tubes to pass through the sealant tape seals. Vacuum was pulled through one flow tube while the other tube was crimped closed. After checking for leaks the crimped tube was opened in a reservoir of epoxy. The epoxy was allowed to flow across the part then both feed tubes were closed. The strut was allowed to fully cure over 24 hours and then was removed from the bagging materials and mandrel and was trimmed to size.

The composite plug was made from approximately 80 1.5" x 1.5" plies of Hexcel 282 3K plain weave carbon fabric and the Araldite LY 8604/Aradur Epoxy Infusion System. The plies were pierced through their centers by and stacked on a perforated metal infusion tube .31" in diameter. End caps were then fitted onto the metal infusion tube's ends to compress the plies to approximately .75" thick. A flow tube was installed in the end of the aluminum tube for the infusion resin. The whole setup is then wrapped in a layer of 1K 5 harness satin fiber glass as a

bleeder with spiral tubing on the inside of this bleeder. The spiral tubing is formed in a ring approximately 2" larger in diameter than the setup containing the carbon plies and is situated concentrically with the metal infusion tube, halfway between the end caps. A flow tube is also attached to the spiral tube. This final setup is bagged in vacuum film and sealant tape with the two flow lines passing through the sealant tape seals. The flow line attached to the metal infusion tube was crimped while vacuum was pulled through the other. After checking for leaks the crimped tube was opened in a reservoir of epoxy. The epoxy was allowed to flow until it filled the spiral tubing attached to the vacuum line. The plug was allowed to fully cure over 24 hours and then was removed from the bagging materials and mandrel and was trimmed to size. To create the mounting hole in the plug, the hole left in the center of the plug from the metal infusion tube was used as a pilot hole for installing a UNC 5/16-18 stainless steel helicoil.

To bond the plug in the strut a fixture was used to hold the plug's mounting hole concentric to the strut. Hysol EA 9394 adhesive was used for the bonding. In trimming the plug, care was taken to insure the outer diameter of the plug was approximately .020" smaller than the inner diameter of the strut to ensure an adhesive bond line thickness of .010." After sanding the mating surfaces with 120 grit abrasive and cleaning, the mating surfaces were generously coated with the adhesive and the plug was slowly inserted while rotating back and forth. The strut was then put under vacuum to help remove air bubbles from the bond line. Afterward, the joint was packed with more adhesive and left to cure for 24 hours in the fixture mentioned above. When installing the strut into the fixture, the plug was pressed inward slightly so its outer surface was approximately .030" below the edge of the strut. After curing the plug end of the strut was sanded flush with the plug and any porosity in the bond line from packing after vacuuming was filled with more adhesive and left to cure for another 24 hours. After the final cure, excess adhesive was sanded away and the strut was trimmed to 8" in length.

3.4 Buffer Materials

Three different types of buffer materials were tested. Aerogel was used in two separate forms: blanket (5) and a loose fill bead pack (6), along with Cryo-Lite (7). Detail about each material is given in Table 4. The aerogel blanket material is a fiberglass batting that is fully embedded with aerogel material. The blanket is made via a proprietary supercritical drying process of the material that leaves a nanoporous aerogel based material. Since the aerogel blanket is encased in the fiberglass batting, no special preparation was required to install it as a buffer. The aerogel beads are made via a similar process to the aerogel blanket, however, without the batting. Since the beads are a loose fill material, they must be contained to act as a buffer. For this testing, a thin nylon mesh was used to contain the beads and was tied off at each end. Figure 14 shows the bead package just prior to being installed in the calorimeter. Cryo-Lite is a special fiberglass based material designed specifically for cryogenic tanks. Testing at the Cryogenics Test Laboratory has shown the parallel direction thermal conductivity to be 3.25 mW/m/K, thus the fiberglass is slightly anisotropic (i.e. the fiber direction conductivity is 70% higher than the normal direction).

Table 4: Buffer material descriptions

Buffer Material	Trade Name	Manufacturer	Avg Thermal Conductivity (mW/m/K)
Aerogel blanket	Cryogel Z	Aspen Aerogels	1.55
Aerogel bead pack	Nanogel granules	Cabot	1.70
Cryo-Lite	Cryo-Lite	Lydall/Manning	1.95

Note: Average thermal conductivity based on KSC testing between 293 K and 77 K boundary conditions using Cryostat-100, and was measured in the normal direction.



Figure 14: Aerogel bead package

3.5 Test Matrix

The test plan was developed to investigate several of the major variables associated with MLI and the integration with various penetrations. The general test matrix is given in Figure 15. The worst case scenario was assumed to be the no integration case, where a hole is left in the MLI for the penetration, but no attempt is made to prevent conduction from the penetration to the MLI. Both buffers and temperature matching were tested to determine the flexibility of the two methods (i.e. different environmental temperatures) in multiple applications.

Multiple materials were tested as a buffer: aerogel blankets, aerogel beads, and Cryo-Lite fiberglass blankets. The aerogel blankets and Cryo-Lite fiberglass blankets were tested at two different diameters, 0.5" (0.25" on the radius) and 1.0" (0.5" on the radius). The aerogel beads were install in a nylon sleeve and tested at a thickness of approximately 0.5" (0.25" on the radius).

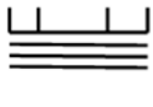


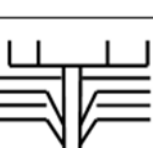
Test	Test Description	Reason	Figure
1	No Penetration	Baseline	
2	No Integration a) Without gap b) With gap (a no buffer case)	Worst Case	
3	Isolated Penetration a) 1/2" Aerogel Blanket b) 1/2" Bead Pack c) 1" Aerogel Blanket d) 1/2" CryoLite e) 1" CryoLite	Isolate bulk insulation from penetration insulation	
4	Temperature Matched a) Lockheed b) Test #1	Best Case (assumes single warm temperature)	
5	Variable Size a) 0.25" strut with best from above b) 5a. disturbed MLI c) 1" strut with best from above	Change size of strut	
6	Composite Strut a) Isolated b) No Adaption	Change penetrations conductivity	

Figure 15: General Test Matrix for Penetrations Calorimetry

To determine the temperature matching, two different scenarios were used. The first was to use the Lockheed Equation for double aluminized Mylar and silk net (treated) to determine the temperature gradient through the MLI (8). The National Institute of Standards and Technology's Cryogenic Material Property database was used to determine the temperature gradient through penetrations of aluminum and fiberglass epoxy (G-10, normal) using a 20 node model (9). The location where layers 1, 3, 8, 16, and 25 should meet the penetration was determined based on these calculations. Also, in the first few tests, the actual temperature profiles of the MLI and the penetration were measured. These measurements were used to calculate the location where layers 3, 8, 16, and 25 should meet the penetration for the second "Test #1" test. Layers 3, 8, and 16 were chosen because they are approximately equidistant along the temperature profile (~50 K apart) as can be seen in Figure 16.

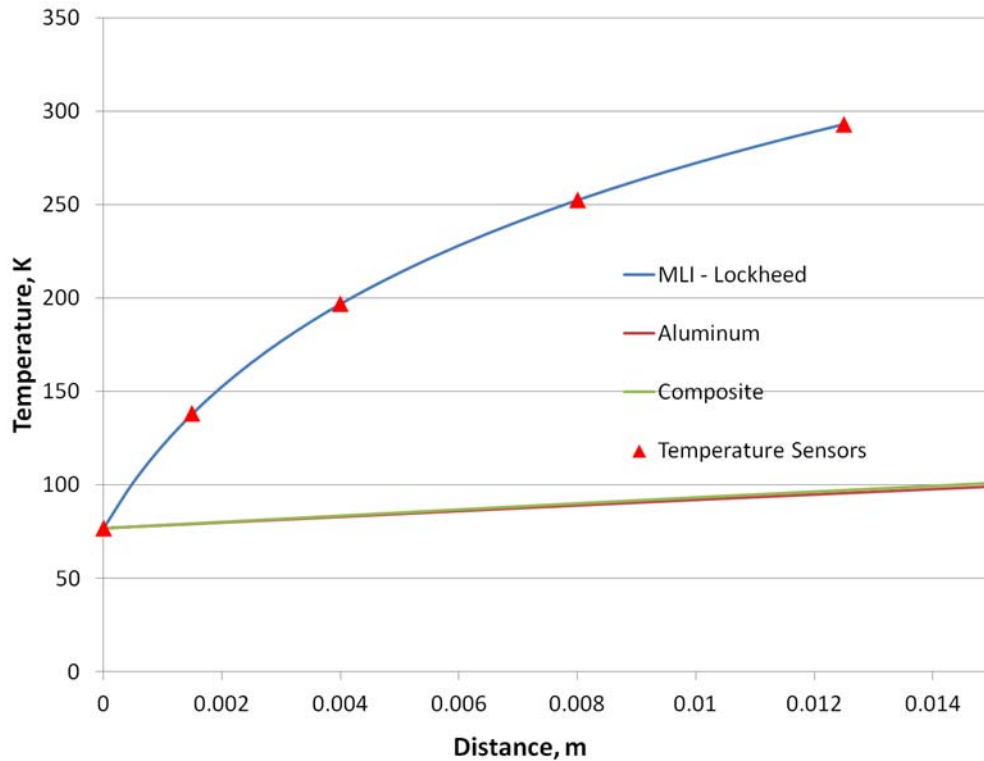


Figure 16: Temperature profile of MLI and penetrations through the thickness of the MLI

3.6 Experimental Uncertainty

The uncertainty was calculated using root sum squared method using the allowable calibration and other instrumentation uncertainty and equations for heat transfer and thermodynamics. The analysis assumes the measurement is representative of the heat transfer from the test article. That means 1) that the cryostat's design eliminates heat transfer to the test chamber from sources other than the penetration and test section of MLI, and 2) that nothing but heat input is affecting the boiloff rate of nitrogen such as impurities, changes in atmospheric pressure, or other factors that are unknown. Because the system is dependent on nonlinear formulas, the uncertainty changes from test to test. Table 5 shows the uncertainty for a representative test. The full uncertainty analysis is contained Appendix C.

Table 5: Uncertainty Analysis Results

		Test	Test P101	
		MLI Serial Number	SN 002	
		Description	1/2" strut, no buffer	
	Related Parameter	Units	Relative Uncertainty Ux/x	Nominal Value
Thermal Conductivity	k	W/m-K	0.005	138.3
Volumetric Flow Rate	Vmeas	sccm	0.05	744.1
Volumetric Flow Rate	VMLI	sccm	0.05	31
Density	ρ	Kg/m ³	0.0223	1.167
Heat of Vaporization	h_{fg}	kJ/kg	0.02	199.2
Length of Heat Transfer	x	m	0.0019	0.18603
Area of Strut	A	m ²	2.75E-04	3.04E-05
Temperature Difference	ΔT	K	0.0261	108.5
Total Heat Leak	-	W	-	3.079
MLI Heat Leak	-	W	Test P100	0.13
Strut Heat Leak	-	W	-	2.45
Total Uncertainty			0.0101	
Percent Uncertainty			2.022%	

3.7 System Data

This section gives a broad overview of all the data collected on each test in order to allow for a better understanding of the more brief data presented later as well as the operations of the testing.

One of the main measurements taken is the boil-off (or mass) flow coming out of each chamber of the cold mass. Figure 17 shows the flow meter data for both the guard and test chambers for a typical test. Additionally, the liquid fill level is shown. The liquid level is calculated by integrating the flow over time and is solely for the purpose of knowing when the chambers need to be refilled. For Cryostat-600, the guard chamber needs to be kept at roughly 20% full minimum to ensure that the test chamber is always submerged in liquid nitrogen. The flows were generally very steady and had a slight variance with fill level. In order to calculate the heat load, the test flow rate is averaged over a long period of time (typically at least several hours, often approaching a day) and is multiplied by the density of the vapor at standard temperature and pressure and the heat of vaporization of the liquid at the saturation pressure.

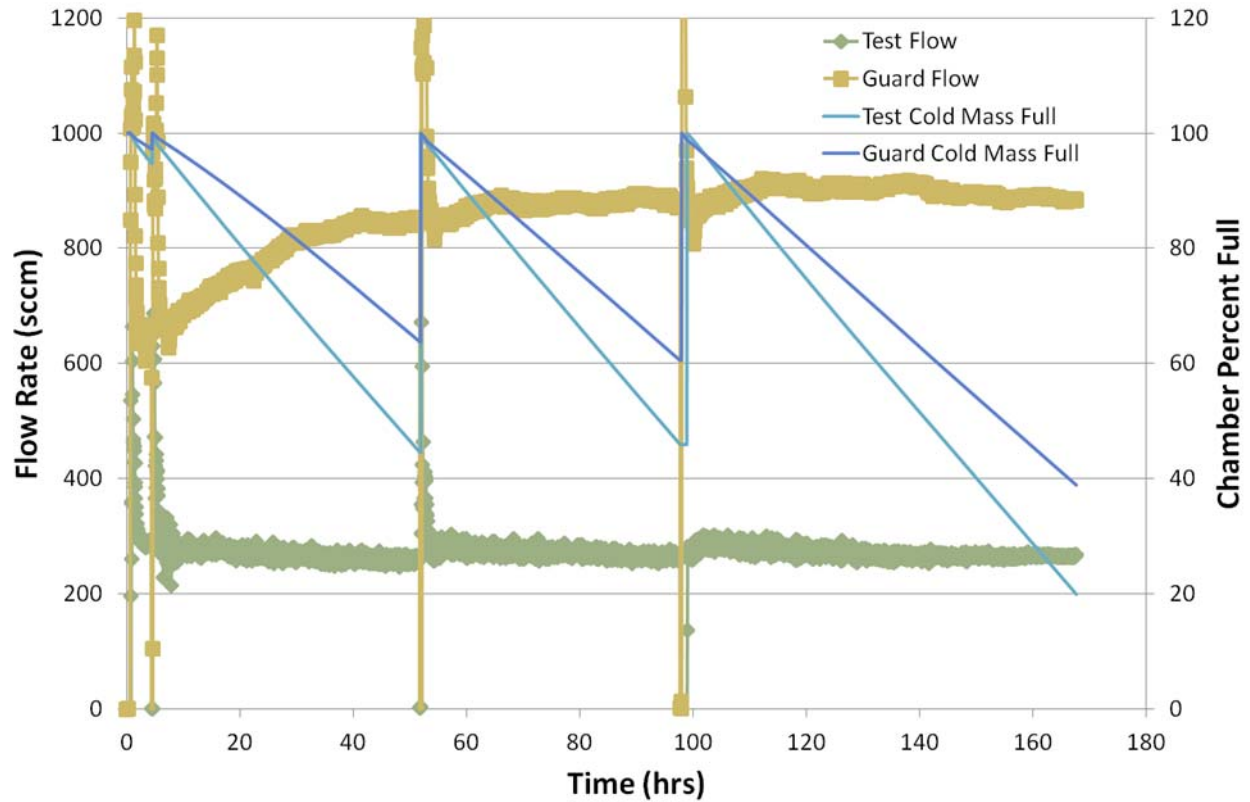


Figure 17: Typical mass flow rates and fill level data

The other main data measured is the temperature data and vacuum chamber pressure. Figure 18 shows the system temperatures on the cold mass and penetration as well as the vacuum chamber pressure. T1 – T3 are on the cold mass as shown in Figure 7. At about the 5.5 hour mark in Figure 18, the liquid nitrogen is refilled. This re-chills the top of the cold mass and also causes some disturbances in the vacuum pressure due to the cryopumping and subsequent off-gassing of the system associated with pouring the cold liquid through the vent/fill lines. However, after several hours the pressure levels off well below 10^{-6} torr. The strut temperatures (T4-T7) were slightly affected by the refill but not greatly so.

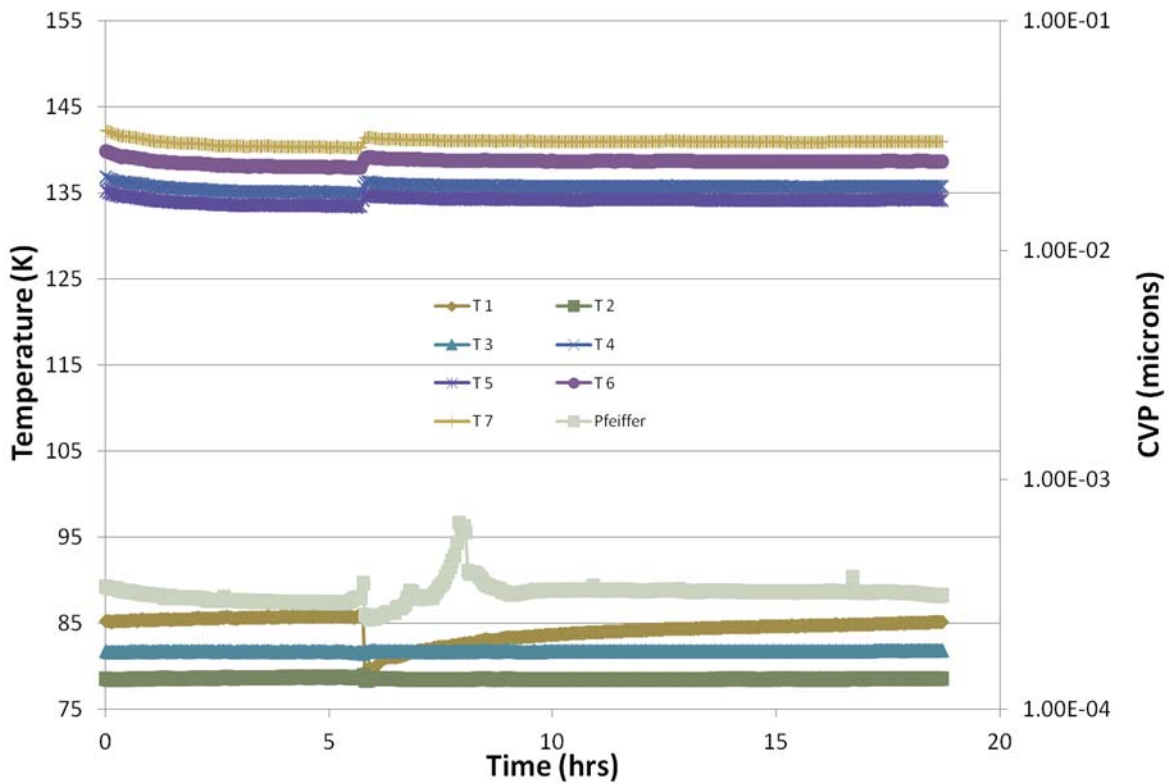


Figure 18: Typical system temperatures and preferences

Figure 19 shows a representation of typical MLI temperatures as a function of time. It can be seen that after roughly 5 hours, the temperatures leveled off and the temperatures are steady with a few exceptions during which refills occur. Figure 20 shows the same data, except instead of being plotted versus time, the averaged measurement of each sensor during steady state is plotted versus location within the MLI. Thus the dark blue line is the temperatures on the warm layer of MLI, the light blue line is the temperatures on the 16th layer from the cold side, and so on. For which temperature represents which data point position, please refer to Figure 8. Layer one is the closest layer to the cold mass. This is the main data representation that is used to show the degradation radius.

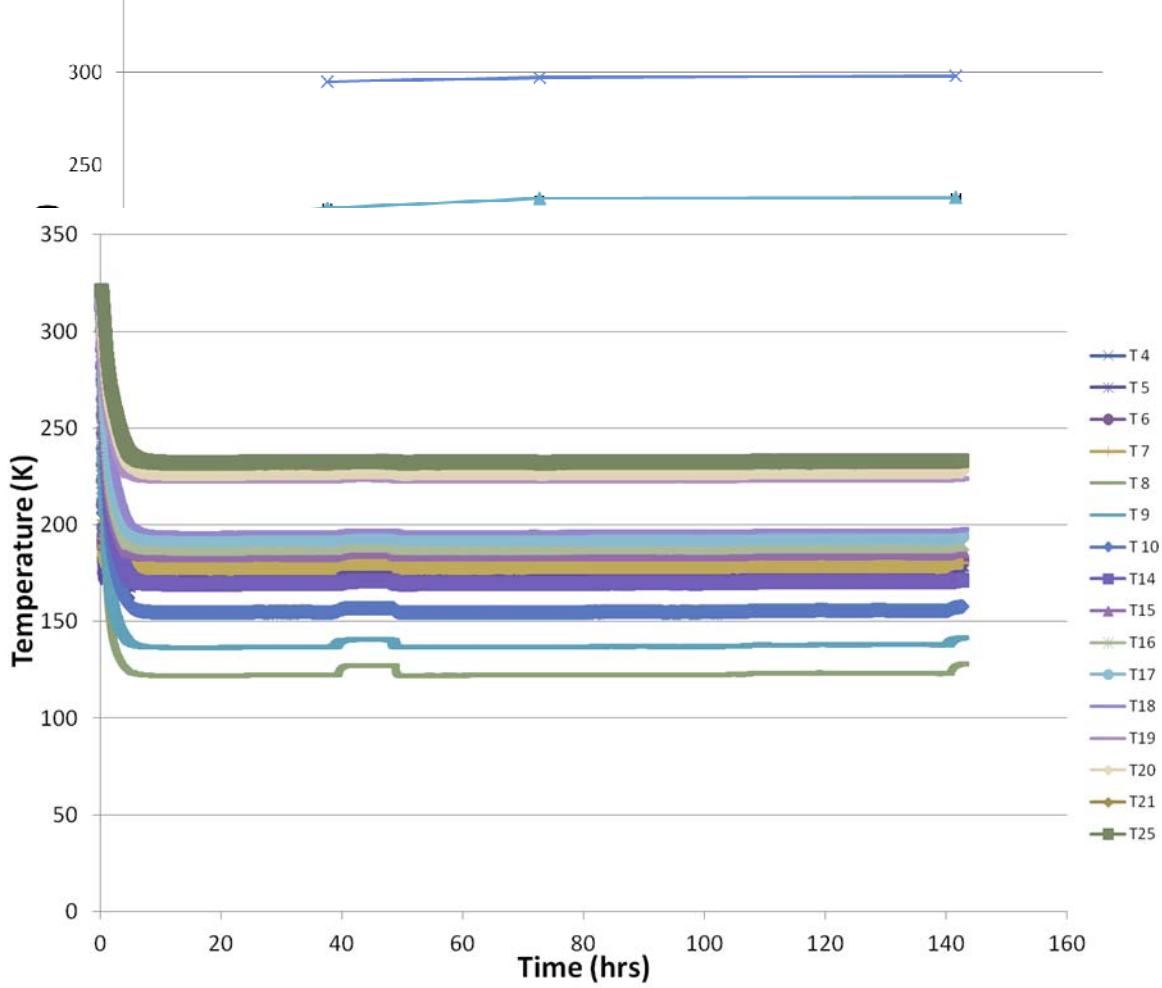


Figure 19: Typical MLI temperatures

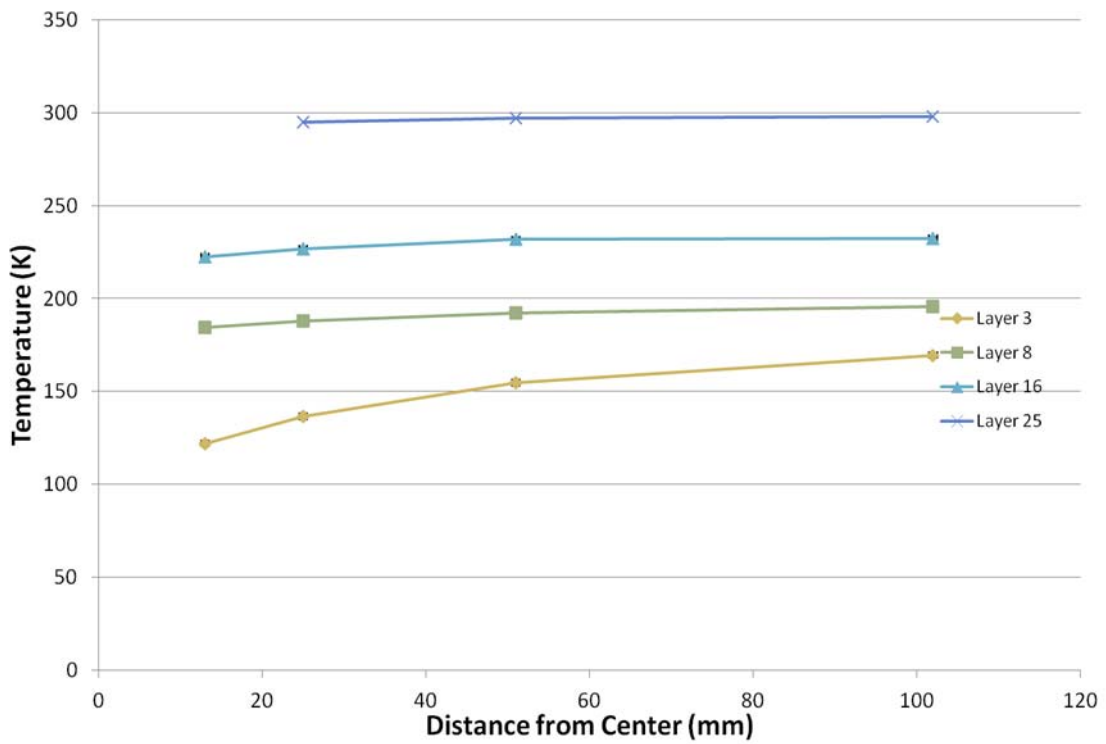


Figure 20: Steady state MLI temperatures plotted vs. location

4 Thermal Models

Thermal models were developed in Thermal Desktop and run on Sinda/Fluint to allow for scaling of the test results to larger struts and different boundary conditions. The models were anchored to the testing performed in this report. This section describes the thermal models.

4.1 Model Overview

Two models were created, a detailed model of the C-600 cold mass that was used for validation of approach and a model that was used to scale those results to flight applications. The detailed model included both of the liquid chambers, the edge guard, penetration, MLI test sections, and other detailed components of the testing. Its purpose was to develop and validate a method for modeling the penetration issue. The flight scaling model was a much more basic investigation that used the same method developed in the detailed model but didn't include the details of the calorimeter, instead looked at a much more basic and open configuration where edge effects were basically ignored.

Material properties for most of the components used in these models are included in the table below. A thermal conductivity and emissivity as a function of temperature was used for most of these materials, the table gives values for these at one temperature for reference.

Table 6: Material properties used in the calorimeter thermal model

Component	Material	Property	
		Thermal conductivity (W/m-K)	Emissivity
Aluminum Strut	Aluminum 6061	k = F(T), 86.6W/m-K at 88.7K	ε= F(T), 0.0275 at 80K file: Unpolished Aluminum
Composite Strut	Carbon Fiber Epoxy	k = F(T), 1.1W/m-K at 120K file: IM2/977-2	ε= 0.8 file: IM2/977-2 Graphite Epoxy
Cold Mass	Stainless Steel 304L	k = F(T), 8.11W/m-K at 80K file: Stainless Steel 304L	ε= F(T), 0.128 at 80K file: Stainless Steel 304L Andy
Buffer	Cryolite	k = F(T), 0.00123W/m-K at 150K	ε= 0.953
MLI	Mylar	k = F(T), 0.157W/m-K at 80K file: Mylar	ε= F(T), 0.0246 at 80K file: MLI-Andy2

Most of the material properties were taken from the NIST website; however, for the composite material conductivity the following formula was used:

$$k = 2.49e^{-5}T^2 + 1.84e^{-8}T + 0.57$$

The emissivity used for the carbon fiber epoxy was based on testing at ambient temperature.

4.1.1 Cryostat Detailed Model Overview

The detailed model includes the components of the cold mass including:

- Test and guard chambers
- Insulation surrounding the guard chamber
- Fill tubes

- Penetration
- Penetration insulation
- Passive Heater
- Edge Guard
- Test section of MLI
- G10 MLI support ring

The dimensions of these features were taken from the design drawings. The edge guard is a plastic band, shown in Figure 7, attached to the bottom of the cold mass extending the full thickness of the test MLI. The physical significance of this band is to expose the outer edge of the test MLI to a thermal profile that closely matches its own, limiting heat transfer between the test MLI and other portions of the Cryostat. The G10 ring supports the test MLI and holds it near the cold mass.

Each layer of MLI was modeled as an individual surface. Conduction and convective heat transfer between layers of MLI was modeled using the Lockheed equation (8) to calculate heat transfer between individual nodes on each layer. Temperature dependent emissivity values were used with a multiplier to account for degradation of the MLI. The degradation factor was based on testing at ambient temperature with a sample of MLI that had been used during initial testing.

The test and guard chambers were modeled as boundary nodes connected to the wetted surfaces of the cold mass by LN2 convection. Both chambers were assumed to be 90% full of liquid nitrogen. The Thermal Desktop convection model used assumes no interaction between convective surfaces and a constant temperature across the surface. This is an oversimplification in this case. The model shows a 16K change in temperature across the face of the cryostat for a typical test with a rapid drop moving away from the strut. Table 7 below shows the temperature for a point on the cold mass approximately 25.4mm (1 inch) from the strut centerline. It shows the test side of the cold mass is significantly higher than the LN2 boiling point at atmospheric pressure. This temperature gradient could cause changes in the convective currents that would result in a significant deviation from the constant temperature model used.

Table 7: Typical Cold Mass Temperatures

Test	Total Heat Load (W)	Strut Heat Load (W)	T3 Temperature (K)
P112	0.294	NA	79.984
P115	1.227	0.645	82.716
P116	1.529	0.56	82.445
P117	2.906	2.38	89.047
P106	3.298	2.906	82.075
P103	3.92	3.04	81.383

The guard chamber's fill and vent tubes were modeled with a constant heat load on the top (non-test) surface of the guard chamber. The geometry of the test chamber fill tube was included in the model.

Figure 21 is a cutaway view of the detailed model showing the temperature profile of the area around the strut. The hottest area is the protruding section of the buffer material shown in pink. Not shown in this view is the MLI insulation that surrounds the strut and keeps it at a fairly uniform 150K in the area of the MLI.

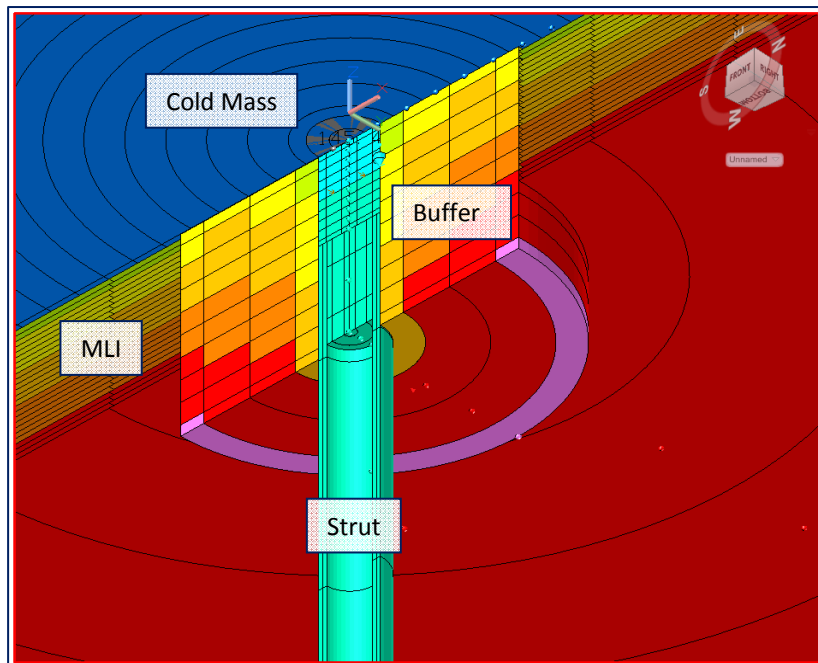


Figure 21: Section View of Detailed Model

4.1.2 *Scaling Model Overview*

A second model was created which did not include the geometry which would not be present in a flight application such as the guard chamber. The model's cold mass was decreased to 2mm

to better simulate a flight application. To keep the model grounded in test data other parameters such as the heat conduction scaling factors between layers of MLI, were retained.

The following cases were considered.

Case	Parameter to Vary	Values	Notes
1	Strut Diameter	6.35mm, 12.7mm, 25.4mm, 50.8mm, 76.2mm, 101.6mm, 127mm, 152.4mm (0.25", 0.5", 1.0", 2.0", 3.0", 4.0", 5.0", 6.0")	12.7mm (0.5") thick Cryolite buffer, 25 layers, Aluminum penetration
2	Buffer Thickness	6.35mm, 12.7mm, 25.4mm (0.25", 0.5", 1.0") Cryolite Buffer	For 76.2mm (3") and 152.4mm (6") penetrations
3	MLI Layers	25, 50, 75, 100 layers	For 76.2mm (3") penetration with 12.7mm (0.5") buffer For 152.4mm (6") penetration with 25.4mm (1.0") buffer
4	Strut Materials	Aluminum, Carbon Fiber	Repeat Case 1 with Composite Repeat Case 2 with 76.2mm (3") composite penetration Repeat Case 3 with 76.2mm (3") composite penetration
5	Cold Boundary Temperature	LN2, LH2	Repeat Cases 1 thru 4 for LH2 temperature at cold mass

4.1.3 Cryostat Detailed Model Validation

The models were validated by comparing the test chamber heat leak, measured by LN2 boiloff, to the model heat leak when the model temperatures matched test conditions. Parameters representing setup conditions such as the amount of contact between the MLI and the cold mass were varied in order to match temperatures between the model and test results. An acceptable match was considered to be an average of 5% as calculated by the following

$$Err_{avg} = \frac{\sum_1^n \frac{abs(T_{test} - T_{model})}{T_{test}}}{n}$$

The following measurements were used for validation

Strut Temperatures		T4, T5, T6, T7
MLI Layer Temperatures	MLI Layer 3	T8, T9, T10, T14
	MLI Layer 8	T15, T16, T17, T18
	MLI Layer 16	T19, T20, T21, T25
	MLI Layer 25	T26, T27, T11

Table 8 below shows how well the model predicted test temperatures along the penetration and in the MLI as well as the predicted change in heat leak due to the penetration compared to actual measurements.

Table 8: Penetration Heat Load Predicted From Model Compared With Test Result Calculations

Test		Average Percent Error In Temperature Match Between Test Results And Model		Change In Heat Load Due To Penetration	
		Strut	MLI	Delta Q – Test (W)	Delta Q – Model (W)
12.7mm AL Strut, 25.4mm buffer	P106 Run 1	1.03%	1.87%	0.262	0.0199
6.35mm AL Strut, 25.4mm buffer	P115 Run 1	1.03%	0.71%	0.288	0.0175
25.4mm AL Strut, 12.7mm buffer	P116 Run 1	0.25%	2.96%	0.656	0.0806
25.4mm AL Strut, 25.4mm buffer	P117 Run 1	0.23%	2.61%	1.135	0.0785
25.4mm Composite Strut, 25.4mm buffer	P121 Run 1	2.13%	1.12%	0.252	0.002

For the model the change in heat load due to the penetration was determined according to the following:

1. Setting the temperature at the warm end of the strut to match the test results by varying the passive heater to strut contact resistance. Normally T7 was used since T13 consistently read high.
2. Changing the contact resistance with the cold mass to match the temperature profile along the strut.
3. Changing the amount of MLI contact with the cold mass to match the temperatures of each of the layers of MLI.
4. The following model results were recorded:

Q_{Total} – sum of heat transferred to the cold mass

Q_{strut} – heat transferred from the strut to the cold mass

5. The model was run a second time without the penetration to determine the baseline heat leak:

Q_{MLI_0} – heat from the unpenetrated MLI

$Q_{\text{MLI}_{\text{Pen}}}$ – heat leak through a strut sized section of MLI

This last term is the amount the heat leak that would have happened through MLI had the strut not been there.

6. The change in heat load was calculated from:

$$\Delta Q_{\text{MLI}} = Q_{\text{Total}} - Q_{\text{strut}} + Q_{\text{MLI}_{\text{Pen}}} - Q_{\text{MLI}_0}$$

The model consistently underestimated the change in heat leak due to the penetration. There are several reasons for this.

1. Penetration Heat Load Calculation

The model gave higher estimates for the penetration contribution to the total heat load compared to the method used to calculate the test data. This is shown in Table 9. During testing the penetration heat load is determined using thermocouple data along the strut in one of two ways.

Test Method 1

The heat load is calculated at a specific point on the strut where the cross-section changes from tubular to solid. Temperature measurements on either side of this transition are used to determine the heat load at the transition by knowing the material properties, strut cross-section, and distance between the measurements. The load at the transition is used as the penetration heat load. Using this method any heat that is transferred between the strut and the buffer is not included in the penetration heat calculation.

Test Method 2

Temperature readings all along the strut are used to determine heat flowing between each set of thermocouples. The average heat load is used as the penetration heat load to the cold mass.

Both methods assume there is no heat transfer to/from the strut other than the passive heater. Both use Fourier's law of conduction

$$Q_{\text{strut}} = kA\Delta T/x$$

Model Method

The model determines the struts contribution to the Test Chamber heat leak by matching the temperatures along the strut just as the second method does but it also accounts for heat transferred between the strut and its surroundings including the buffer and the heat leak through the strut MLI.

Table 9: Penetration Heat Load - Test vs Model

Test		Penetration Heat Load	
		Test (W)	Model (W)
12.7mm (1/2") AL Strut, 25.4mm (1") buffer	P106 Run 1	2.906	0.844
6.35mm (1/4") AL Strut, 25.4mm (1") buffer	P115 Run 1	0.645	0.916
25.4mm (1") AL Strut, 12.7mm (0.5") buffer	P116 Run 1	0.56	0.872
25.4mm (1") AL Strut, 25.4mm (1") buffer	P117 Run 1	1.476	1.78
25.4mm (1") Composite Strut, 25.4mm (1") buffer	P121 Run 1	0.153	0.397

The model shows an appreciable heat exchange between the strut and surroundings. Table 10 shows an example of test data with an aluminum strut compared to model output and the closeness of the model fit between known temperatures. With the exception of T13, the model predicts the strut temperatures fairly accurately.

Table 10: Test P115 Strut Temperature Data

Thermocouple Reference Designation	Test Temperature (K)	Model Temperature (K)	Distance from cold mass (mm)	Estimated Q between temperatures	Estimated Q (W) (From Test Calcs)
T13	263.3	224.6	200	T13 – T7	1.875
T7	189.85	192.8	118	T7 – T6	0.765
T6	167.1	168.6	61	T6 – T5	0.72
T5	153.0	152.2	25	T5 – T4	0.57
T4	146.2	144.5	4		-
Heat to cold mass from strut – Test					0.645
Heat to cold mass from strut - Model					0.916

Another model was created to eliminate uncertainty in the actual penetration heat leak. This model found the change in MLI heat leak by summing the MLI and buffer contributions only. The strut was thermally disconnected from the cold mass and was given a fixed temperature gradient representative of the test results. This model also showed the penetration has a very small effect on the MLI heat leak for buffers 6.35mm (1/4") and thicker.

2. Convection

The standard convection Sinda-Fluent equations used assume the convective surface is contiguous and uniform in temperature or heat flux, however, the tests setup creates a

high heat flux in the center of the cold mass that causes a temperature gradient across the cold mass. That could create changes in the convective currents that would alter the heat transfer to the cold mass. The convective model also treats the guard chamber as a contiguous surface where it should also be modeled as a ring.

Figure 22 shows the predicted temperature across the cold mass along with some actual test data.

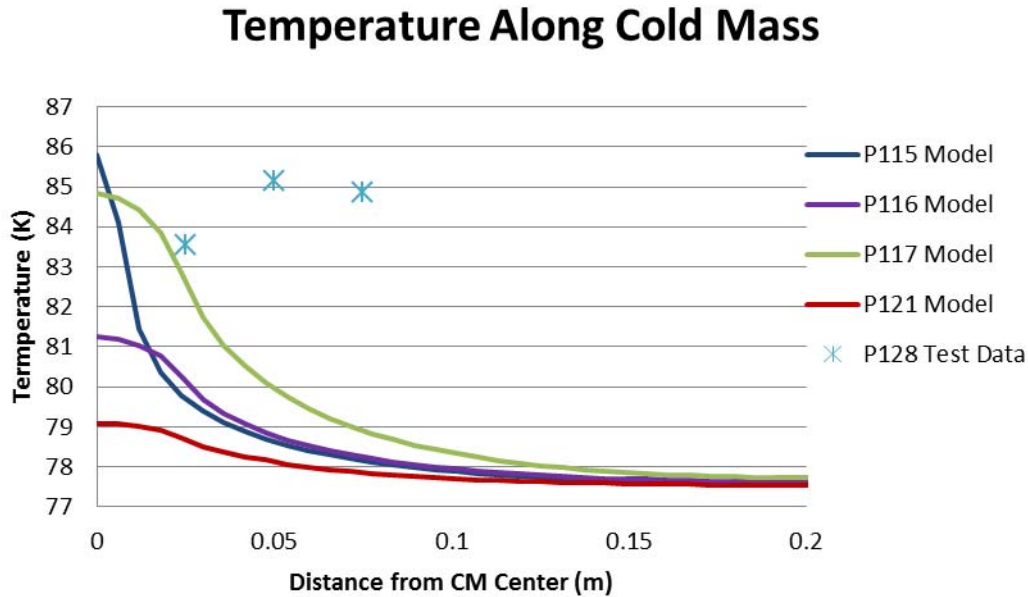


Figure 22: Predicted Temperature Accross Cold Mass

A simplification of the problem is possible where the model includes only the buffer and MLI. The temperature profile of the third layer of MLI is used as the boundary temperature and the temperature profile of the strut is used as another. This avoids uncertainty in convection and conduction along the strut and includes only the portion of the system that is well instrumented but it would only capture the penetrations effect on MLI layers 4 through 25. The effect of the buffer and first three layers of MLI would not be captured.

3. Test – Guard Chamber Heat Exchange

The model shows there is some heat exchanged between the test and guard chambers. The method of calculating the change in heat leak due to the penetration from test results relies on the test and guard chambers being at thermal equilibrium so any heat exchanged results in a bias. For the model the heat exchanged is driven by very slight differences in the temperature along the test section of the cold mass and is on the same order of magnitude as the unpenetrated MLI heat load.

4.1.4 Detailed Model Validation Discussion

MLI Performance

The model and test program may underestimate the effects of the penetration. The tests were performed with a relatively poor performing MLI which did not seem to be in contact with the cold mass for most of the tests. This is evidenced by the relatively low difference in temperatures between layers and the high temperature on layer 3.

Because the MLI stack was at relatively high temperature there was a fairly small gradient between the strut and MLI. In a flight application the penetration may be warmer or colder than the surrounding MLI and so would have a different effect on a better performing MLI.

Test	Strut Temp at Base – T4 (K)	MLI Temp at Layer 3 (K)	MLI Temp at Layer 16 (K)	MLI Heat Flux (W/m ²)
P112	NA	217.9	239.0	8.55
P117	107.3	181.2	261.1	NA

4.1.5 *Scaling Model Results*

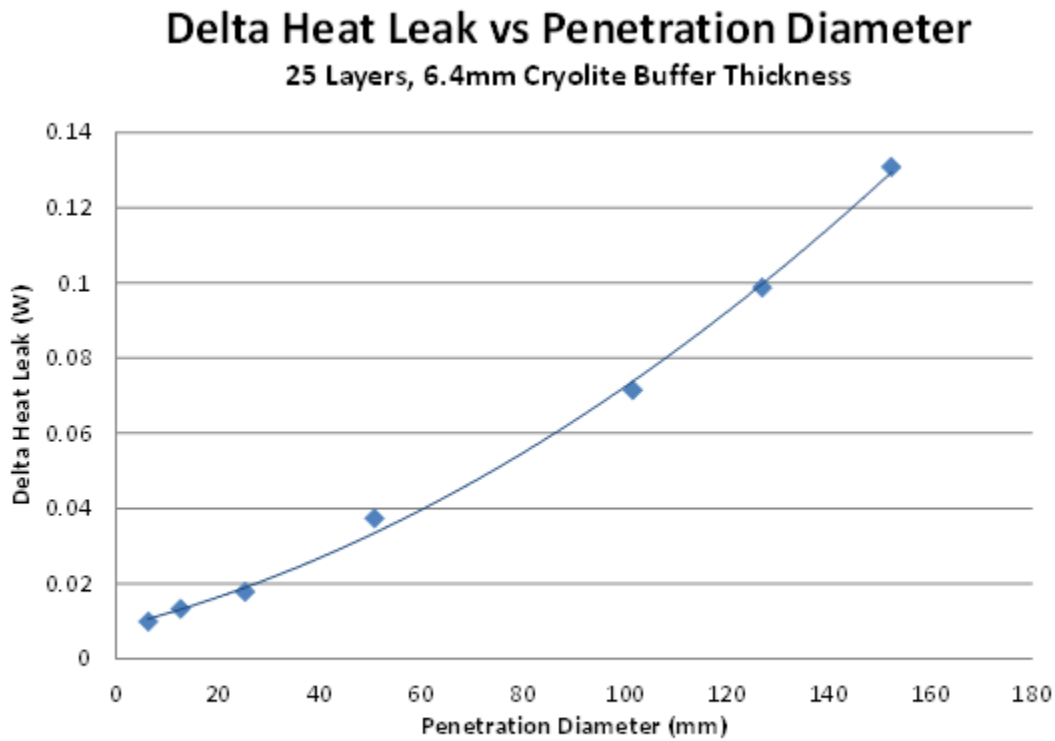
The model was scaled to find the change in the MLI heat leak for conditions that were not tested. The strut was thermally disconnected from the cold mass and the end temperatures were fixed to match a typical temperature profile from the testing, the base of the strut at 150K. The model was run with and without the penetration and the change in heat load was calculated from:

$$\Delta Q_{MLI} = Q_{buffer} + (Q_{MLI} - Q_{MLI_0}) + Q_{MLI_{Pen}}$$

The advantage of this method is that it is independent of penetration parameters such as thickness. The penetration is still thermally connected to the buffer insulation and the remainder of the thermal network is unaffected.

Case 1: Variation of Penetration Diameter

Figure 23 shows the effects of varying the penetration diameter on the MLI heat leak using a 6.4mm (0.25”) Cryolite buffer. The model was run for a cold boundary temperature of 20K and 77K and with composite and aluminum struts. The variation in predicted heat leak between these cases was about the magnitude of the model noise so the figure shows the average of all model runs.

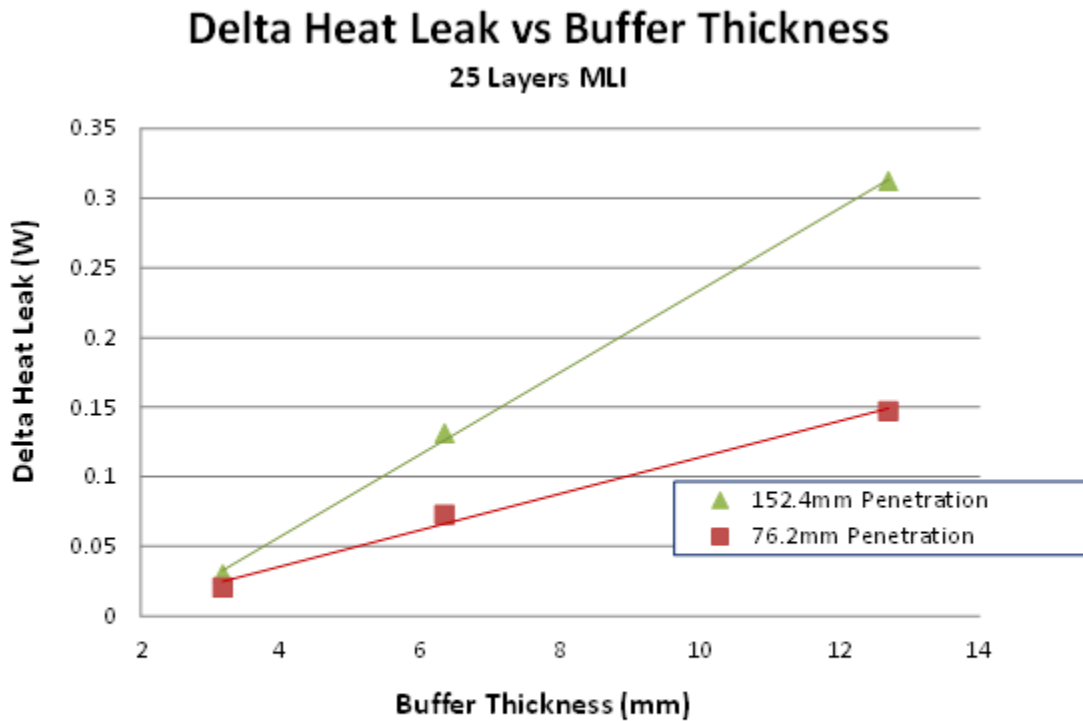


Penetration Details	Change in Heat Leak (W) with Strut Diameter (x in meters)
25 Layers, 6.4mm Cryolite Buffer	$2.95x^2 + 0.346x + 0.00826$

Figure 23: Change in Heat Leak with Penetration Diameter

Case 2: Variation of Buffer Thickness

Figure 24 below shows the effects of varying the buffer thickness around the penetration. Again the base of the strut was held at a fixed temperature of 150K with the strut thermally disconnected from the cold mass. The model was run for a cold boundary temperature of 20K and 77K and with composite and aluminum struts. As with the penetration diameter the variation in predicted heat leak between these cases was about the magnitude of the model noise so the figure shows the average of all model runs.



Penetration and Environment	Change in Heat Leak (W) With Buffer Thickness (x in meters)
152.4 mm Strut, 25 Layers MLI	$Y = 29.5x - 0.0608$
76.2 mm Strut, 25 Layers MLI	$Y = 13.1x - 0.0168$

Figure 24: Change in Heat Leak with Buffer Thickness

Case 3: Variation of MLI Layers

Figure 24: Change in Heat Leak with Buffer Thickness

below shows the effects of varying the number of MLI layers. The model was run for a cold boundary temperature of 20K and 77K and with for both 76.2mm (3 inches) and 152.6 mm (6 inches) aluminum struts.

However for the 76.2 mm strut the variation in predicted heat leak between these cases was about the magnitude of the model noise so

Figure 24: Change in Heat Leak with Buffer Thickness

shows the average of those model runs.

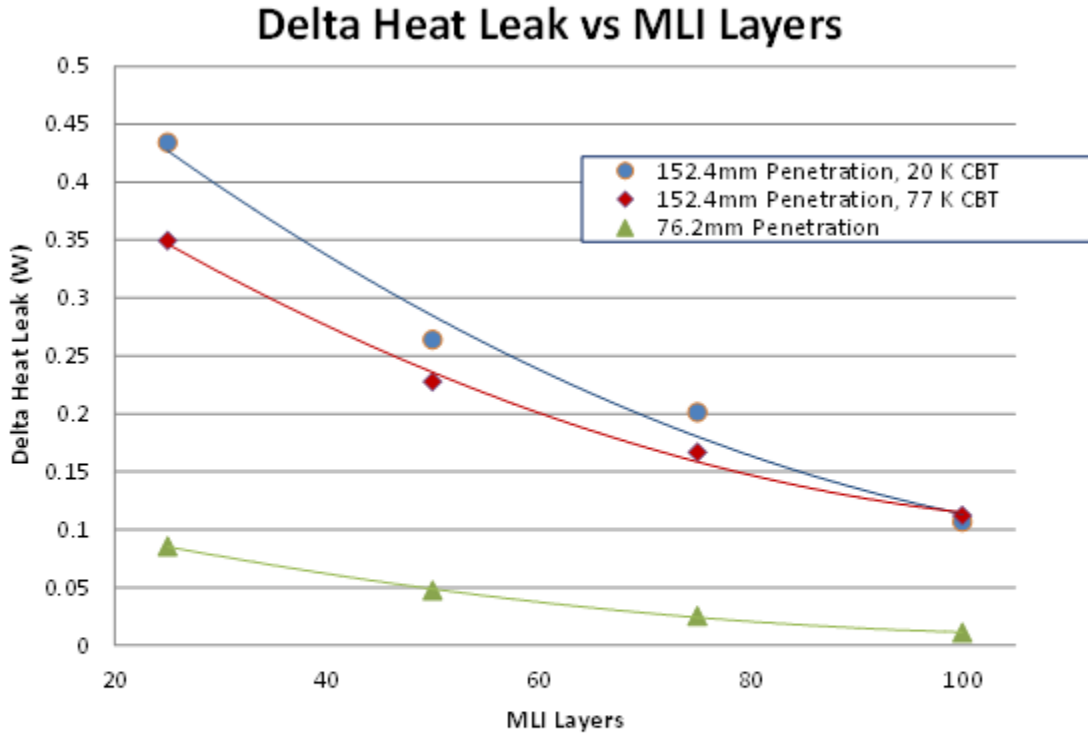


Figure 25: Change in Heat Leak with number of MLI layers

5 Test Results and Analysis

A total of 23 tests were run in order to complete the test matrix in section 3.5, some of these involved subtests where parameters such as the warm boundary temperature was changed or the test was repeated. These tests and the results are summarized in

Figure 26. Six of these tests were no penetration tests, three involved no integration (also known as hot poker), six were involved in the material trade study, two involved temperature matching, six were involved in the strut size analysis, and three tests were run using the composite strut. An additional test was run where the MLI was disturbed to create a non-ideal MLI blanket.

Test #	Test Configurations	Date of Test	Vacuum	WBT	Punch	delta Q	R-affect
			Pressure		Diameter		
			mmITorr	K	(in)	W	mm
P100-1	No Penetration	10 04 11	5.81E-04	291.8	0	-0.005	>100
P101-1	Hot Poker	10 18 2011	7.00E-04	296.7	9/16	0.50	100
P101-2	Hot Poker	10 21 2011	4.70E-04	296.7	1 2/16	0.52	100
P102-1	0.5" strut, 0.5" aerogel blanket	10 26 2011	6.24E-04	300.8	1 2/16	0.779	35
P103-4	0.5" strut 0.5" Cryolite Buffer	11 4 2011	3.10E-04	296.5	1 2/16	0.750	51
P104-1	0.5" strut, 0.5" Vacuum Buffer	11 8 2011	4.09E-04	296.7	1 2/16	0.979	25
P105	0.5" strut, Aerogel Blanket (1")	12 1 2011	3.99E-04	296.5	1 10/16	0.942	35
P106-1	0.5" strut, Cryolite Buffer (1")	12 9 2011	5.71E-04	296	1 10/16	0.262	<25
P107	No Penetration	11 18 2011	2.34E-04	297.2	0	0	
P108	0.5" strut, Aerogel Bead Pack(1")	12 16 2011	1.36E-03	297	1 10/16	0.759	<25
P109	No Penetration	12 22 2011	5.12E-04	297.5	0		75
P110-2	Temp Matched - LM, 0.5" strut	1 12 2012	7.72E-04	297.6	1 1/16	0.759	>100
P111-2	Temp Matched - TD, 0.5" strut	1 24 2012	1.85E-03	296.6	1 1/16	0.01	50
P111-4	Temp Matched - TD, 0.5" strut	1 26 2012	9.30E-04	330.8	1 1/16	0.570	100
P112	No Penetration	1 31 2012	7.10E-04	297.3	0	0	25
P113	0.25" strut, 0.5" cryolite buff	2 8 2012	7.98E-04	296.9	14/16	0.200	25
P114	0.25" strut, 0.5" cryolite buff, disturbed	2 15 2012	4.57E-04	297.01	14/16	0.264	25
P115	0.25" strut, 1" buffer	2 22 2012	7.36E-04	296.6	1 5/16	0.288	< 25
P116	1.0" strut, 0.5" buffer	2 28 2012	7.53E-04	297.3	1 10/16	0.680	>100
P116-2	P116 at high temp	3 5 2012	1.18E-03	325.4	1 10/16	0.783	>100
P117	1.0" strut, 1.0" buffer	3 8 2012	6.25E-04	297.2	2	0.986	>100
P118	No Penetration	3 15 2012	2.41E-03	297	0	0.000	
P119	Composite Strut no buffer	3 22 2012	1.09E-03	296.3	1 1/16	0.305	>100
P120	Composite Strut, 0.5" cryolite buffer	3 30 2012	5.97E-04	296.9	1 10/16	0.256	51
P121	Composite strut, 1.0" cryolite buffer	4 9 2012	4.89E-04	296.9	2	0.252	35
P122	No Penetration	4 16 2012	5.42E-04	295.9		0.000	

Figure 26: Test Result Summary for Penetration Calorimetry

5.1 No Penetration – Null testing

Prior to punching a hole in any MLI blanket, a null test was run to determine the no penetration heat load. Temperature sensors were installed in the blanket per Figure 7 to get baseline data for temperature gradients in these particular undisturbed MLI blankets. The results for the no penetration testing are shown in Table 11. It is interesting to note the apparent dependence of the heat load based on the diameter of the blanket. However, the temperature profile of P100 (see

Figure 27) shows that the edges of the layers were shorting to the versify edge guard. Figure 28 (temperature profile of P118) shows that by removing the outer 5 mm or so, that shorting was generally avoided, though there are still some gradients and edge effects. When the diameter of the sample was kept the same, the heat loads were repeatable within 6% for nearly identical blankets. This was an important result as it removes any biasing of the test data based on null blanket variations.

Table 11: No penetration MLI test results

Series #	Blanket Serial Number	Outer Diameter (mm)	Heat load (W)	Blanket Usage
P100	SN2	305	0.130	Buffer Materials
P107	SN3	305	0.122	None
P109	SN5	300	0.203	Temperature Matching
P112	SN6	285	0.294	Penetration Sizes
P118	SN3	295	0.194	Composite Strut
P122	SN7	300	0.191	Retesting

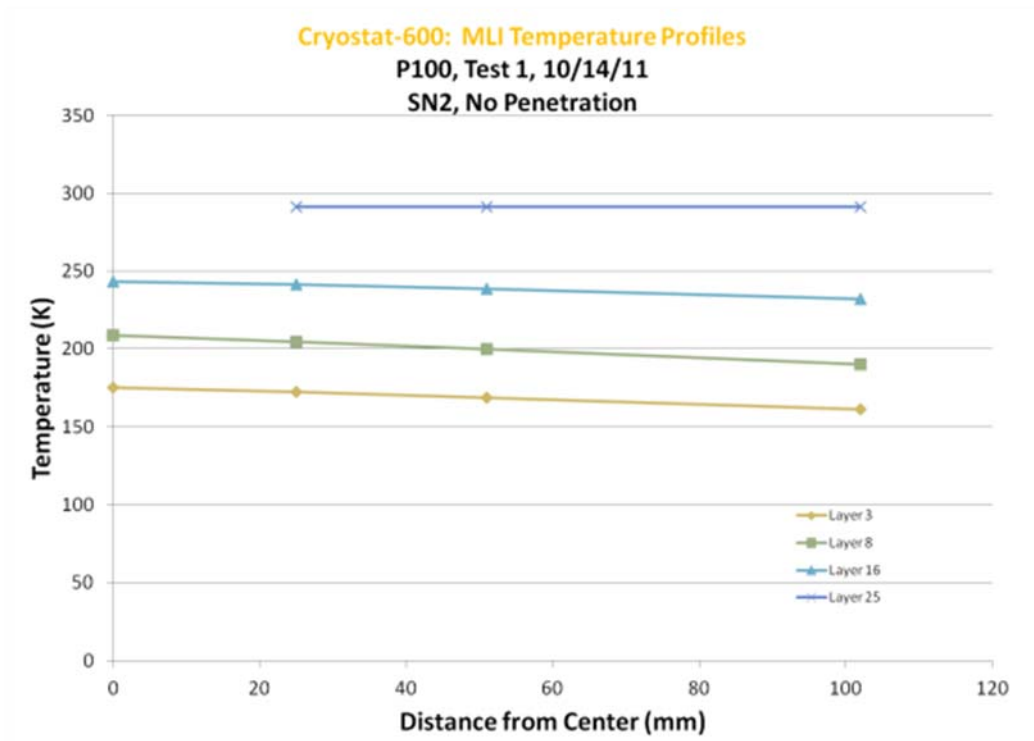


Figure 27: Temperature Profile for P100

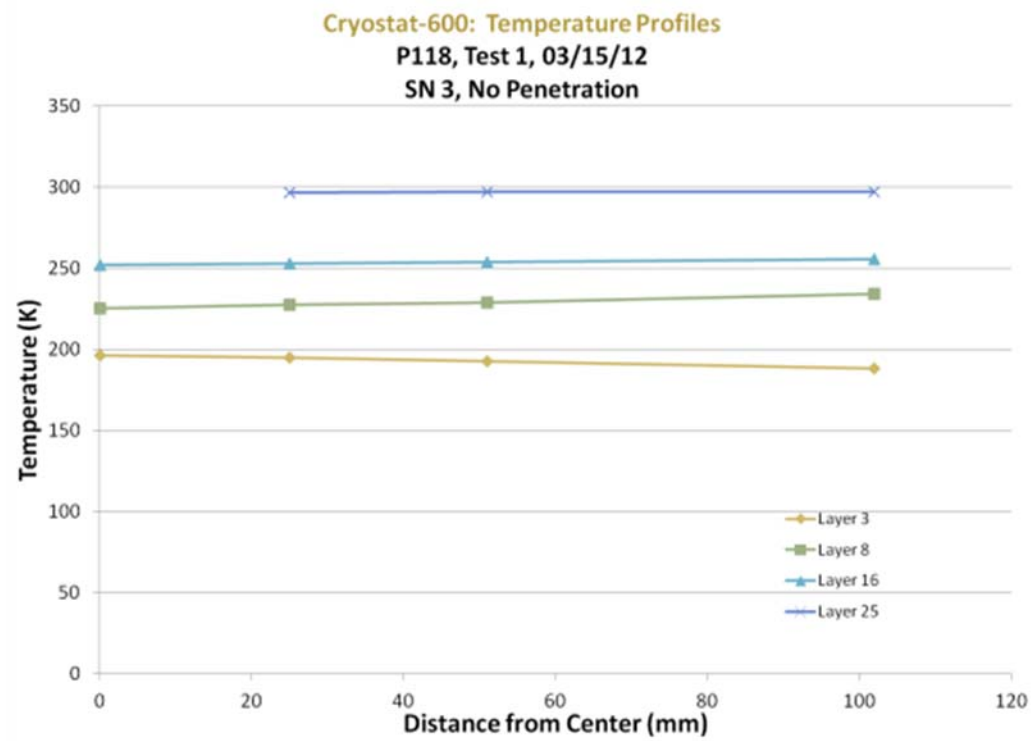


Figure 28: Temperature Profile for P118

5.2 No Integration

No integration testing was run with both aluminum and composite struts. For the aluminum strut, a 0.0159 m (0.625 inch) hole was punched through the MLI blanket which the 0.0127 m diameter strut was placed. The 0.0259 m (1.020 inch) diameter composite strut was placed through a 0.0270 m (1.063 inch) hole in the MLI blanket. The delta heat load was 0.50 W from the aluminum strut and 0.31 W for the composite strut. The degradation radius was over 100 mm for both tests. The temperature profiles for the aluminum strut are shown in Figure 29. The No Integration testing served as a general reference point as what was thought to be the worst integration method to prevent degradation of the blanket. However, based on the test data, it is clearly better than too large of a buffer or a buffer that is not highly pliable, but is not as good as a properly sized buffer.

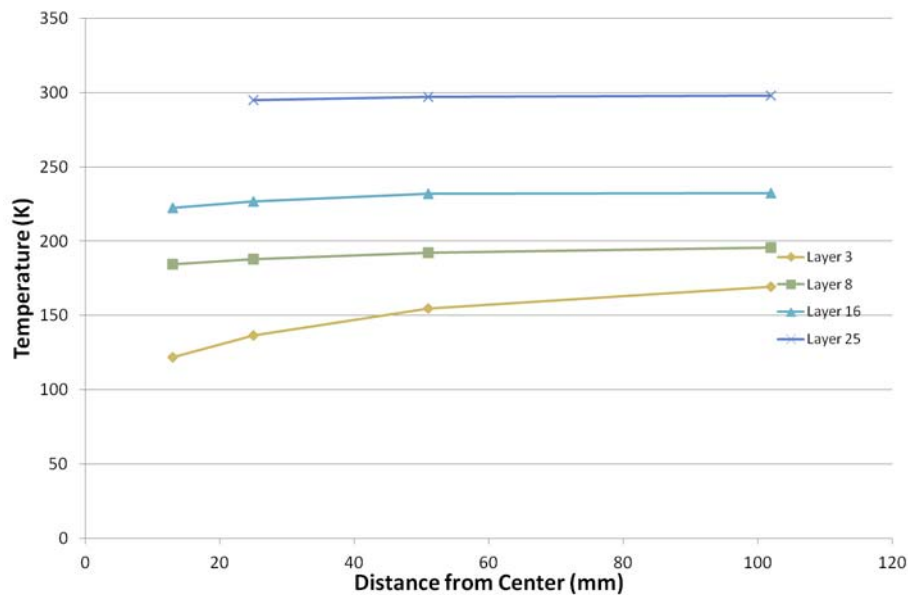


Figure 29: Temperature profiles for No Integration testing on Aluminum strut

5.3 Buffer Materials

Buffer material testing was performed using the 0.5" aluminum penetration. The penetration was wrapped with four layers of MLI when not within the MLI/buffer area. Three different materials and various thicknesses were tested at two different sizes (0.5" diameter, and 1.0" diameter). Additionally the 0.5" diameter (0.25" radius) buffer was tested with no fill material, essentially a vacuum buffer. Based on the performance of P106, the Cryo-Lite system was determined to be the best performing. However, all insulation systems outperformed the vacuum buffer case. Figure 30, Figure 31, and Figure 32 show the different materials installed as a buffer.

During the buffer testing, it was noticed that the degradation radii was not necessarily related to the integration thermal losses. This is because the buffer allows heat load through it while it isolates the MLI from the strut. Thus the buffer operation is a function of how well it thermally isolates the MLI from the penetration in addition to the thermal properties of the buffer. So a buffer material that has better surface contact properties (i.e. less thermal contact), yet a higher thermal conductivity, could provide a better overall result as that material could be installed in a thinner application.

In addition to outperforming the other materials thermally, Cryo-Lite was also the easiest material to handle. It can be easily squeezed down to fit within the cut out hole, allowing it then to puff back out and completely fill the hole. The aerogel blankets and bead pack could not completely refill the hole, and thus were susceptible to cracks forming between the buffer material and the MLI blanket. This pliability in combination with less material to thermally touch with the MLI surfaces made the Cryo-Lite the best performing material.

Table 12: Results from buffer material testing at different buffer thicknesses

Material	ΔQ at 0.5" (W)	ΔQ at 1.0" (W)
Aerogel Blanket	0.764	0.942
Aerogel Beads	N/A	0.759
Cryo-Lite	0.75	0.262
Vacuum	0.979	N/A



Figure 30: Aerogel blanket buffer - 0.5" (0.25" radius)

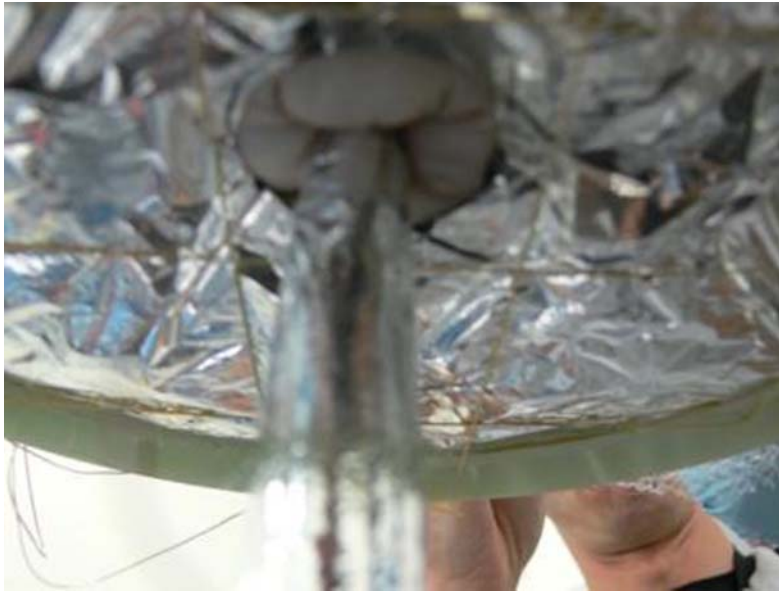


Figure 31: Aerogel beads packed in nylon and installed on calorimeter

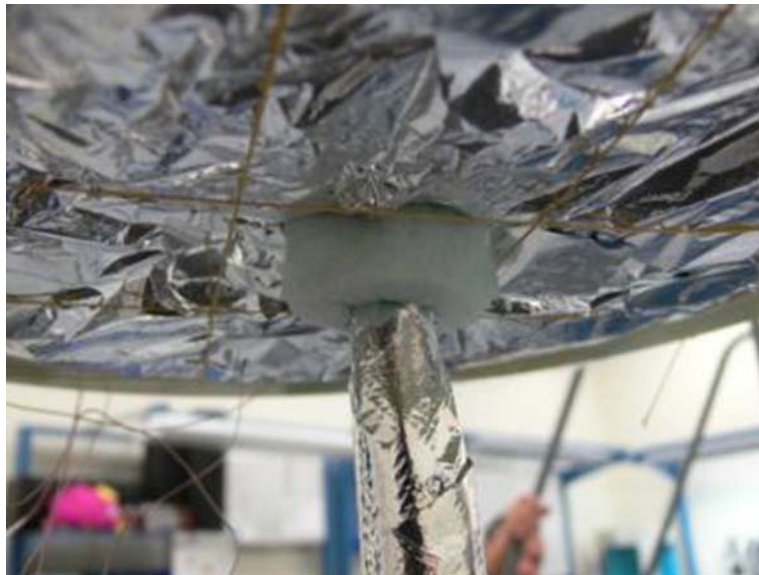


Figure 32: 1" (0.5" radius) Cryo-Lite buffer

Following the materials trade study, testing was done on multiple sized penetrations. The penetrations are described in section 3.3. Aluminum struts of 0.25" and 1.0" were added to the 0.5" tests already performed. Cryo-Lite total thicknesses of roughly 0.5" and 1.0" were tested on each strut. Figure 33 shows a typical two dimensional temperature profile for the buffer testing, where generally the impacted area was very small.

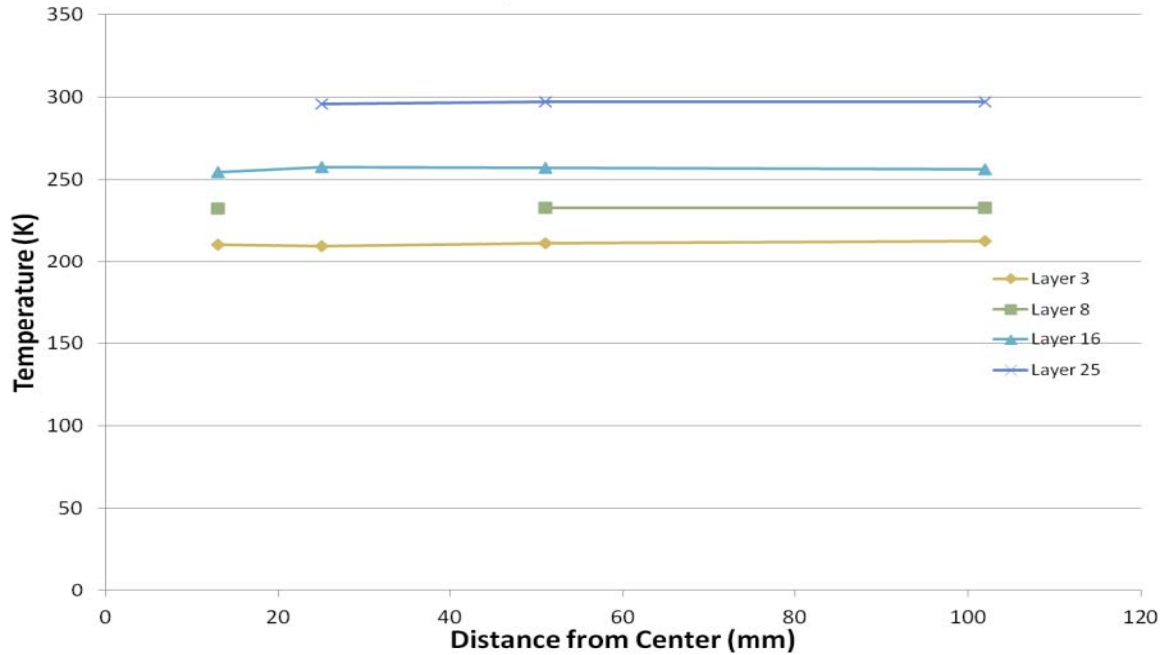


Figure 33: P115, 1 inch buffer, 0.25" strut 2-D thermal projection

Table 13 shows the test results for the various sized penetration cases. It is noted that there was much more uncertainty with the 1" aluminum penetrations because the temperatures of the struts were colder as the warm boundary temperature was not able to be maintained on the strut, but was maintained on the MLI. The top section shows the test numbers, the middle section the parasitic heat loads, and the bottom section shows the degradation radius. The results indicate that the Cryo-Lite material is best suited for use as a thin material to isolate the penetration from the MLI. For the 0.25" penetration, the testing shows that a quarter inch thick radius buffer is sufficient and that larger thicknesses hurt performance. However, for the larger penetrations, the half inch radius buffer appears to be closer to the optimal thickness. The degradation radius appears to be within 2 penetration diameters on the preferred thicknesses.

Table 13: Test Results for Cryo-Lite Buffers on various penetration sizes

Aluminum 6061-T6		Buffer Thickness/radius, in	
struts Test log		0.25	0.5
Strut Size, OD (in)	0.25	P113	P115
	0.5	P103	P106
	1	P116	P117

Aluminum 6061-T6		Buffer Thickness/radius, in	
struts, dQ		0.25	0.5
Strut Size, OD (in)	0.25	0.200	0.288
	0.5	0.750	0.262
	1	0.680	0.986

Aluminum 6061-T6		Buffer Thickness/radius, in	
struts, R effect		0.25	0.5
Strut Size, OD (in)	0.25	25	< 25
	0.5	51	<25
	1	>100	>100

To assess the performance of the Cryo-Lite buffer across variable environments, the P116 configuration was run at a warm boundary temperature of 330 K. To account for the null MLI heat load difference, the subtracted out load was multiplied by the ratio of warm boundary temperatures raised to the fourth power. The resulting parasitic heat load increased from 0.68 W in the 297 K test to 0.78 in the 325 K test, and increase of 15%. The degradation radius still was greater than 100 mm, so no change was seen. If these two tests are used to create a power factor for Warm Boundary Temperature, then the exponent solves to 1.56 yielding the equation:

$$\frac{Q_{T=325}}{Q_{T=297}} = \left(\frac{325}{297} \right)^{1.56}$$

Additional testing with buffers was done on the composite strut. With the 0.5" buffer, a parasitic heat load of 0.256 W was measured with a degradation radius of 51 mm. With the 1.0" buffer, a parasitic heat load of 0.252 W was measured with a degradation radius of 35 mm. There was little thermal benefit from increasing from the 0.5" to the 1.0" around the composite strut. However, the composite strut showed much lower thermal penalties than the aluminum strut. This is due mostly to the lower thermal conductivity of the strut itself.



Figure 34: Composite strut installed on calorimeter with a Cryo-Lite buffer

5.4 Temperature Matching

Temperature matching is the analytically optimal method for integrating a penetration into an MLI blanket. It involves determining the temperature gradients through the installed MLI blanket as well as along the penetration and then cutting an adapter to attach the MLI to the penetration where the temperatures are the same. Table 14 shows a summary of the temperature matching locations.

Temperature gradient predictions were run prior to any testing (see Figure 35) using the double aluminized mylar, double silk netting Lockheed equation for the MLI temperature gradients and NIST data of Aluminum 6061-T6 and G10 (composite) for the penetration temperature gradients (8) (9). The MLI was done on a layer by layer basis (25 layers), while the penetrations were each done in with 21 nodes and 20 even conductors, assuming a constant cross section the length of the penetration. The warm boundary was assumed to be 293 K, the cold boundary 77 K, and the interstitial pressure 5×10^{-6} torr. The layer density of the MLI was assumed to be 20 layer/cm.

Following the initial no penetration testing of both SN2 (P100) and SN6 (P112), the actual temperature gradients through the MLI, as well as along the penetration (from P110), were compiled and used to determine where the adaptations between the MLI and penetration should be. Figure 36 shows the temperature gradients through the MLI for the Lockheed predicted case in addition to P100 and P112. In addition to testing the “As Measured” temperature matching at a warm boundary temperature of 293 K (the design temperature), the warm boundary temperature was ramped up to 325 K to test off-nominal conditions of the temperature matching and assess the flexibility of temperature matching.

Table 14: Temperature matching locations along the strut (total length .203 m)

Layer #	Lockheed Strut Location (m)	As Measured Strut Location (m)
1	0.020	N/A
3	0.046	0.076
8	0.102	0.140
16	0.157	0.178
25	0.203	0.203

Note: As measured test did not include layer 1

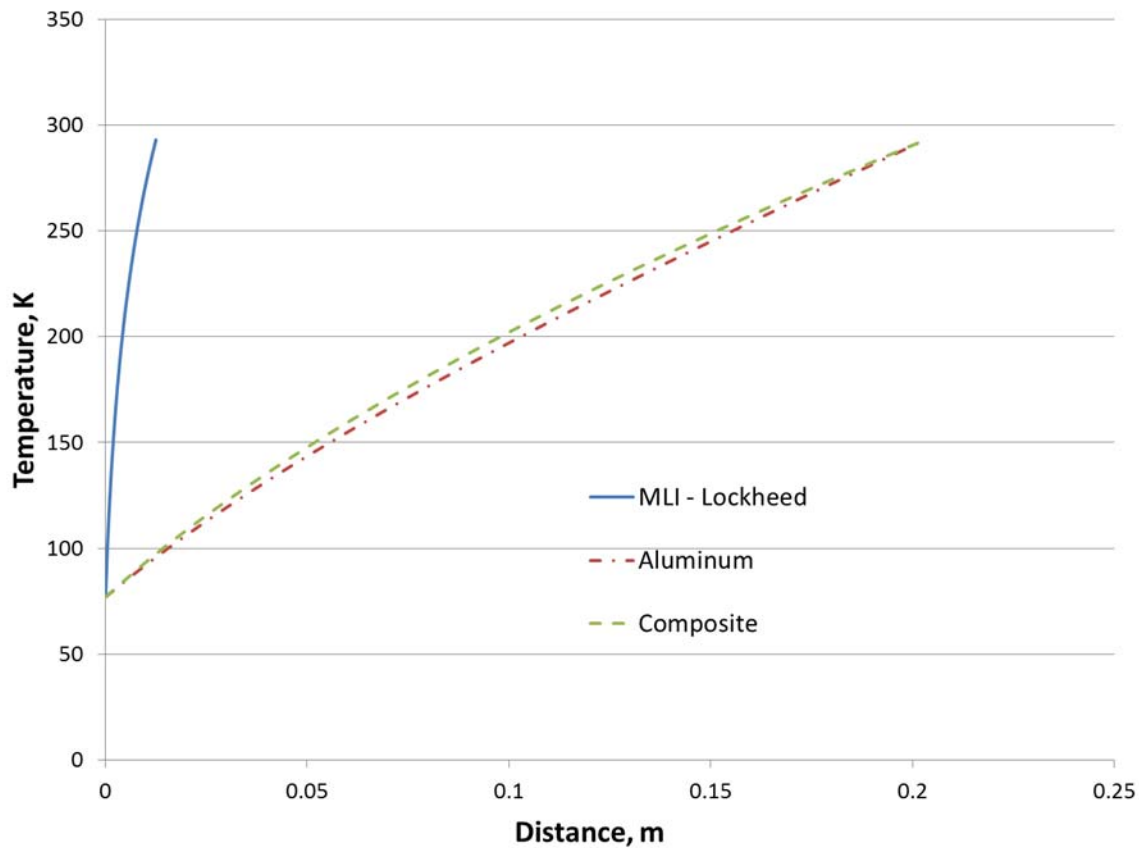


Figure 35: Predicted MLI and penetration temperature gradients

The initial testing of the Lockheed and NIST temperature matched sample showed a heat penalty (ΔQ) of 0.75 W. Testing of the “As Measured” temperature matched sample shows a much lower heat penalty of 9.5 mW. This suggests that equations used did not adequately predict the temperature gradients of both the MLI and the penetration. Contact resistance was neglected between the penetration and the cold mass. This may have played a role in the

errors on the penetration side, but as shown in Figure 36, the MLI temperatures were off as well.

When the environment of the “As Measured” sample was changed to a warm boundary temperature of 325 K, the heat penalty increased from 9 mW to 0.57 W. This shows that changing the environmental temperature, even only 30 K, can drastically affect the performance of the temperature matched penetration.

In theory temperature matching is ideal, however, since conduction and radiation heat transfer vary to different powers of temperature, in general a temperature matched solution can only be applied at a single environmental temperature. For locations where the temperature might greatly change (such as in low earth orbit), this appears to have unintended consequences in off-nominal conditions.

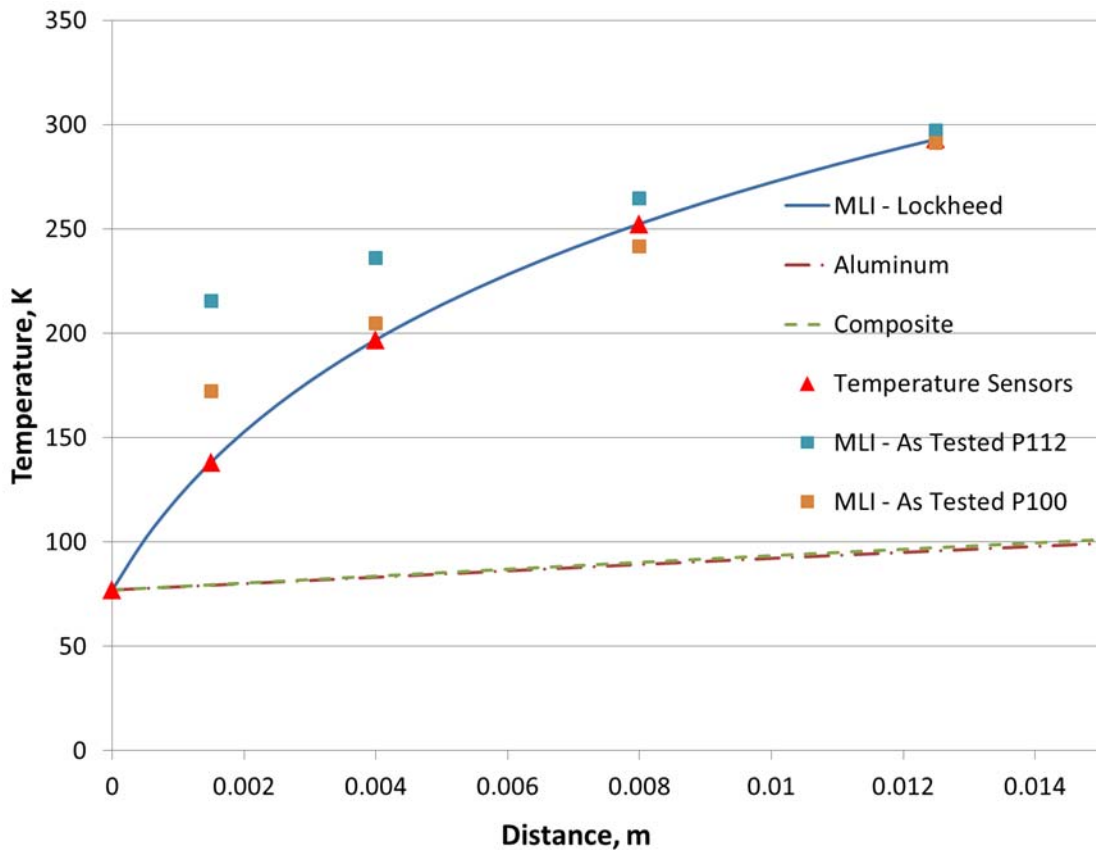


Figure 36: Temperature gradients through MLI showing predicted, P100, and P112. Also shown for reference are the strut temperatures.

6 Conclusion

Over twenty-three tests were run to help characterize the thermal performance impacts of penetrating MLI. Testing included the development and fabrication of a new calorimeter and test method for two dimensional thermal performance testing. The testing included null testing of every blanket, no integration testing, buffer testing, and temperature matching testing with different size and material penetrations. The preferred method of isolating penetrations was shown to be the buffer method, and Cryo-Lite the best material to use as a buffer. The thermal degradation or parasitic heat load was shown to be a function of strut diameter, buffer thickness, buffer material, warm boundary temperature, and penetration material. The buffer method was shown to be easier to develop, more robust, and less variable over multiple conditions and environments.

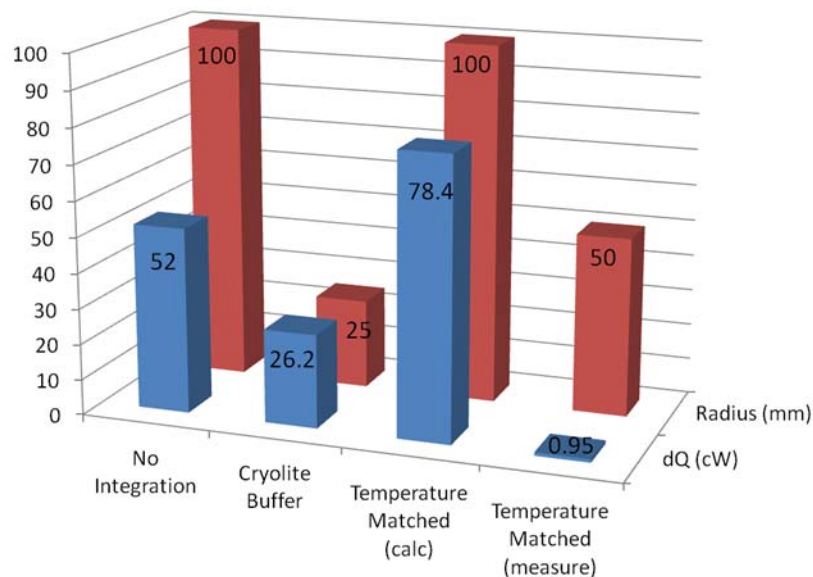


Figure 37: Comparison between different integration methods for a half inch aluminum penetration

Similarly, a thermal model was developed and validated against the test results. The model was then used to extrapolate predictions to systems that are larger than could be tested in the current set up. While an overall mathematical model could not be developed, a set of representations were developed for the main driving variables. These equations should be used to determine specific cases by using the ratio of a single chosen case and the actual case in each of the plots compared to the reference data point (using a 6.4mm thick Cryolite buffer and either a 152.4 or 76.2 mm penetration). Since the same buffer thickness is not enveloped between the penetration diameter (

Figure 23) and number of layers (

Figure 24: Change in Heat Leak with Buffer Thickness

), the second reference point is required. The second reference point can be used on either of the two graphs, but it is shown on the number of layers calculation. T_h should be in the units of Kelvin.

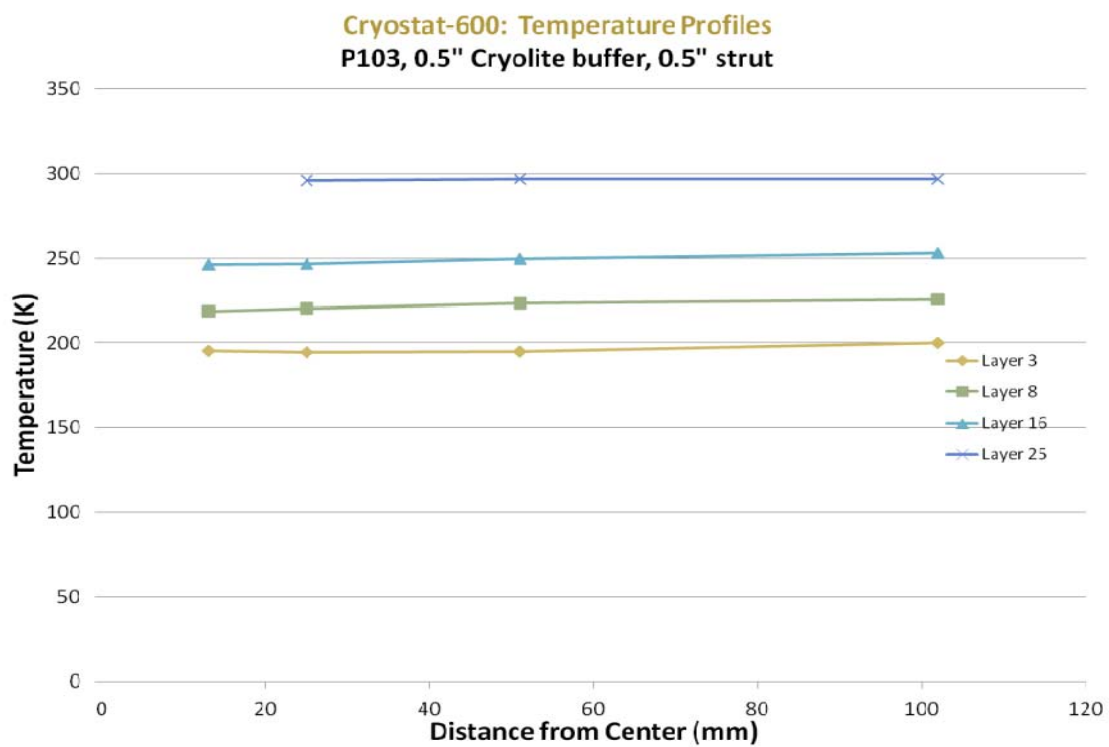
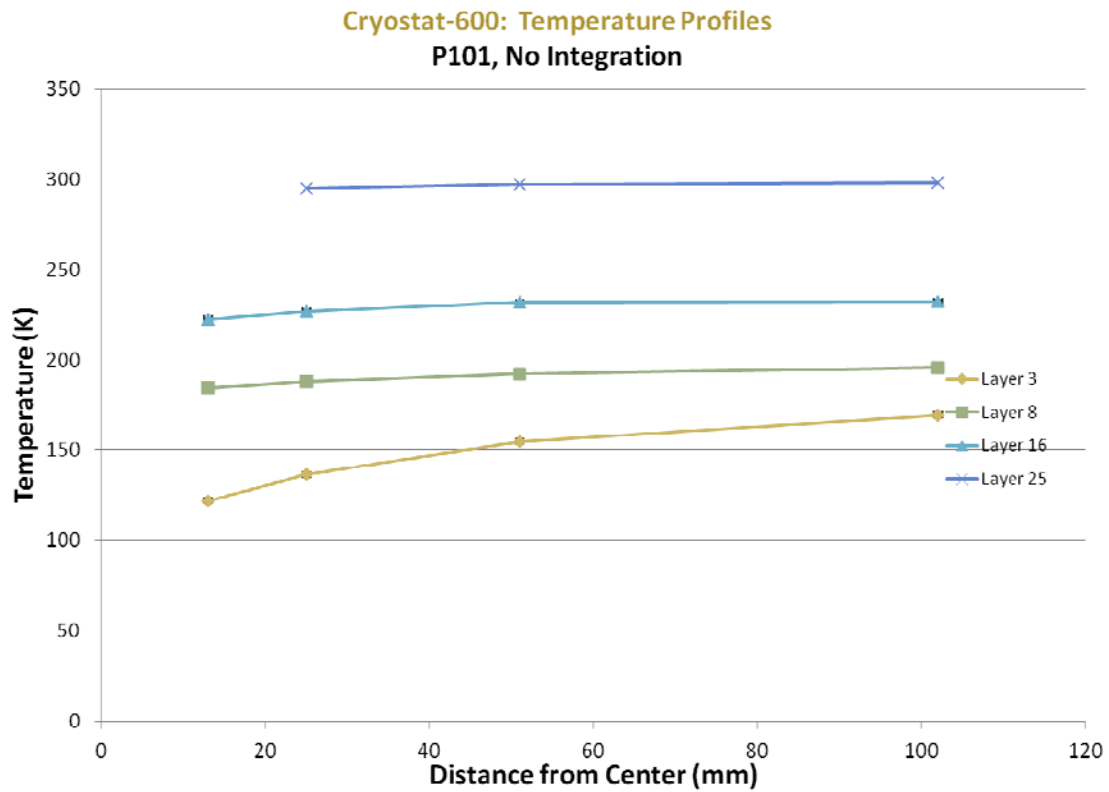
$$dq = q_{ref} \left(\frac{q_{actual}}{q'_{ref}} \right)_{\#layers} \left(\frac{q'_{ref}}{q_{ref}} \right)_{buffer\ thickness} \left(\frac{q_{actual}}{q_{ref}} \right)_{diameter} \left(\frac{q_{actual}}{q_{ref}} \right)_{buffer\ thickness} \left(\frac{T_h}{297} \right)^{.64}$$

Thus an overall approach to the integration of penetrations into MLI blankets has been developed. Thermal modeling was anchored to testing on a modified flat plate calorimeter. This is readily usable for designing and preliminarily specifying designs for cryogenic systems.

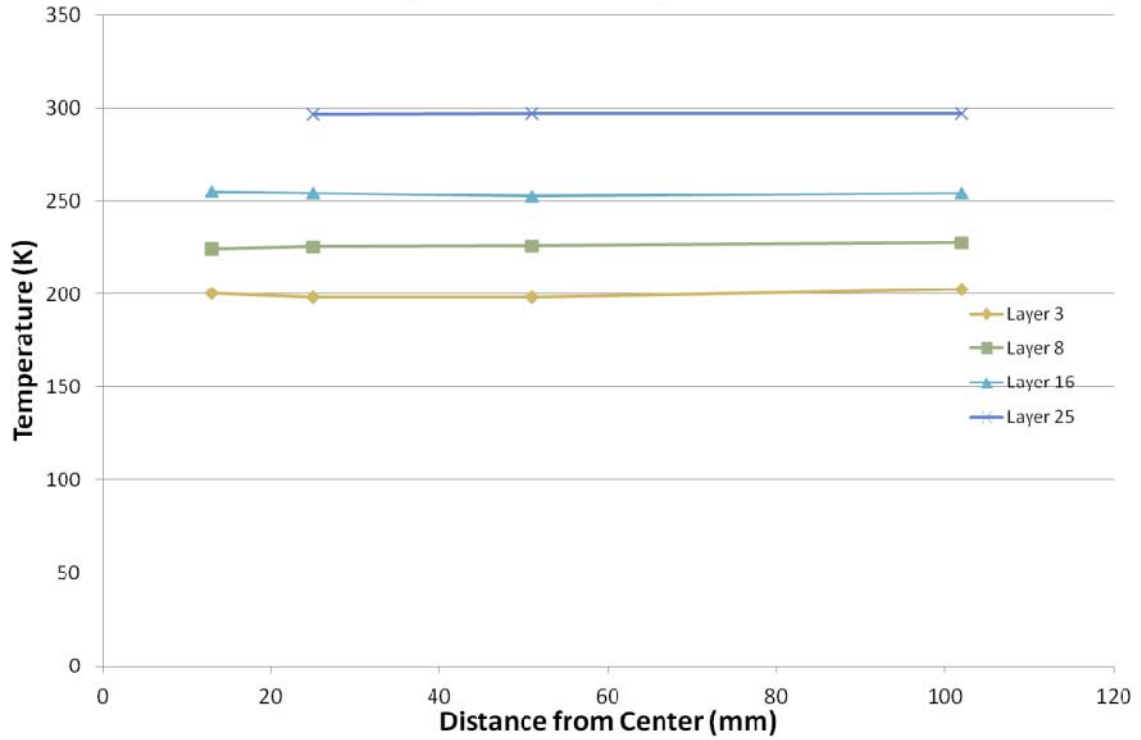
References

1. **Coston, R. M., Murray, D. O. and Lambert, L.** *A Study On High-Performance Insulation Thermal Design Criteria*. Sunnyvale, CA : Lockheed Missiles & Space Company, 1967. pp. 42-104. LMSC-A847882, Vol. I.
2. **Sumner, I. E.** *Degradation of a Multilayer Insulation Due to a Seam and a Penetration*. Cleveland, OH : Lewis Research Center, 1976. TN D-8229.
3. **Johnson, W. R. and Sprague, E. L.** *Analytical Investigation of Thermal Degradation of High Performance Multilayer Insulation in the Vicinity of a Penetration*. Cleveland, OH : National Aeronautics and Space Administration, Lewis Research Center, 1968. NASA TN D-4778.
4. **Lord Corporation.** Aeroglaze Z306 Polyurethane Coating. [Online] Lord Corporation, 2012. [Cited: March 23, 2012.] <http://www.lord.com/products-and-solutions/coatings/product.xml/611>.
5. **Coffman, B. E., et al., et al.** Aerogel Blanket Insulation Material for Cryogenic Applications. [book auth.] J.G. Weisend II. *Advances in Cryogenic Engineering Vol. 55B*. NY : American Institute of Physics, 2010, pp. 913-920.
6. **Koravos, J. J., et al., et al.** Nanogel aerogel as a load bearing insulation material for cryogenic systems. [book auth.] J. G. Weisend II. *Advances in Cryogenic Engineering, Vol 55B*. Melville, NY : American Institute of Physics, 2010, pp. 921-927.
7. **Johns Manvill Corporation.** [Cited: July 9, 2012.] http://www.jm.com/engineered_products/hpi31_cryolite.pdf.
8. **Keller, C. W., Cunnington, G. R. and Glassford, A. P.** *Thermal Performance of Multi-layer Insulations, Final Report*. Sunnyvale, CA : Lockheed Missile and Space Company, 1974. Contract NAS3-14377.
9. Cryogenic Technologies Group - Material Properties. *NIST Material Measurement Laboratory*. [Online] National Institute of Standards and Technology. [Cited: March 23, 2012.] <http://cryogenics.nist.gov/MPropsMAY/material%20properties.htm>.

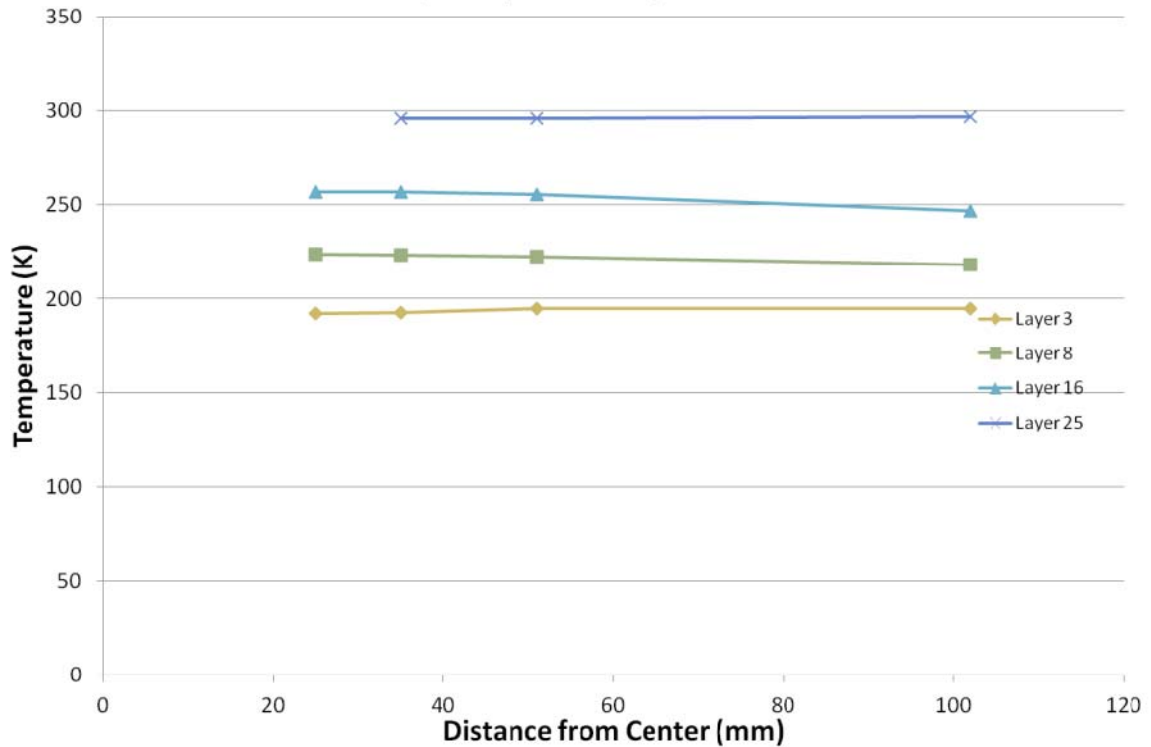
Appendix A – More data plots



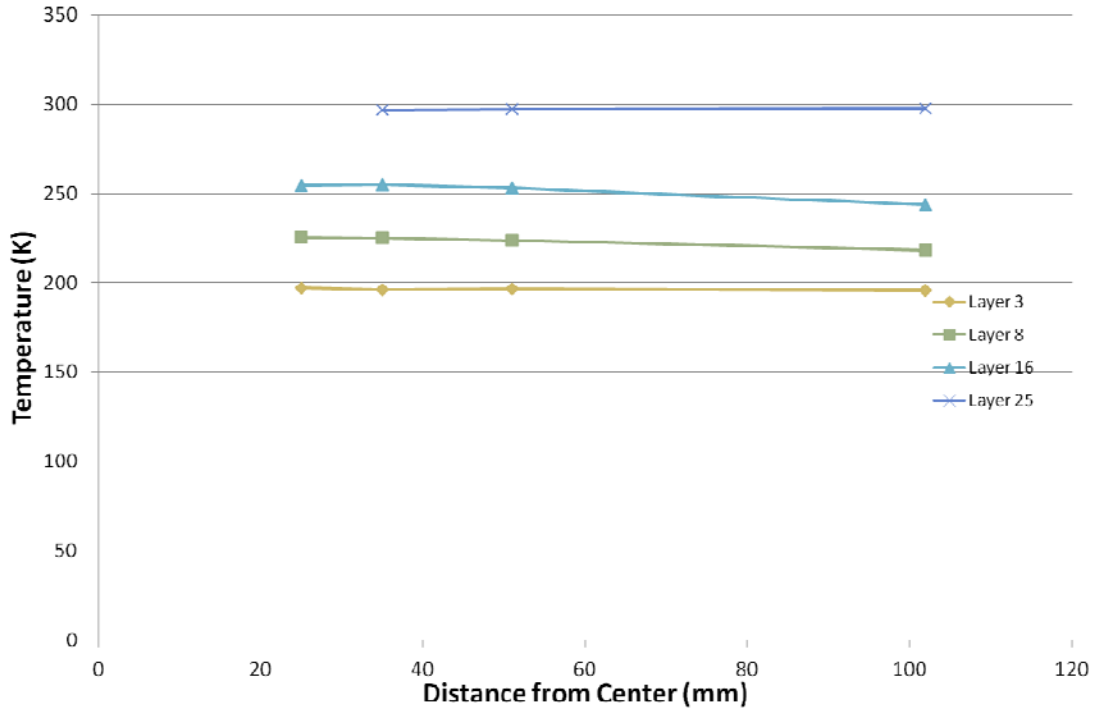
Cryostat-600: Temperature Profiles
P104, 0.5" Vacuum Buffer, 0.5" strut



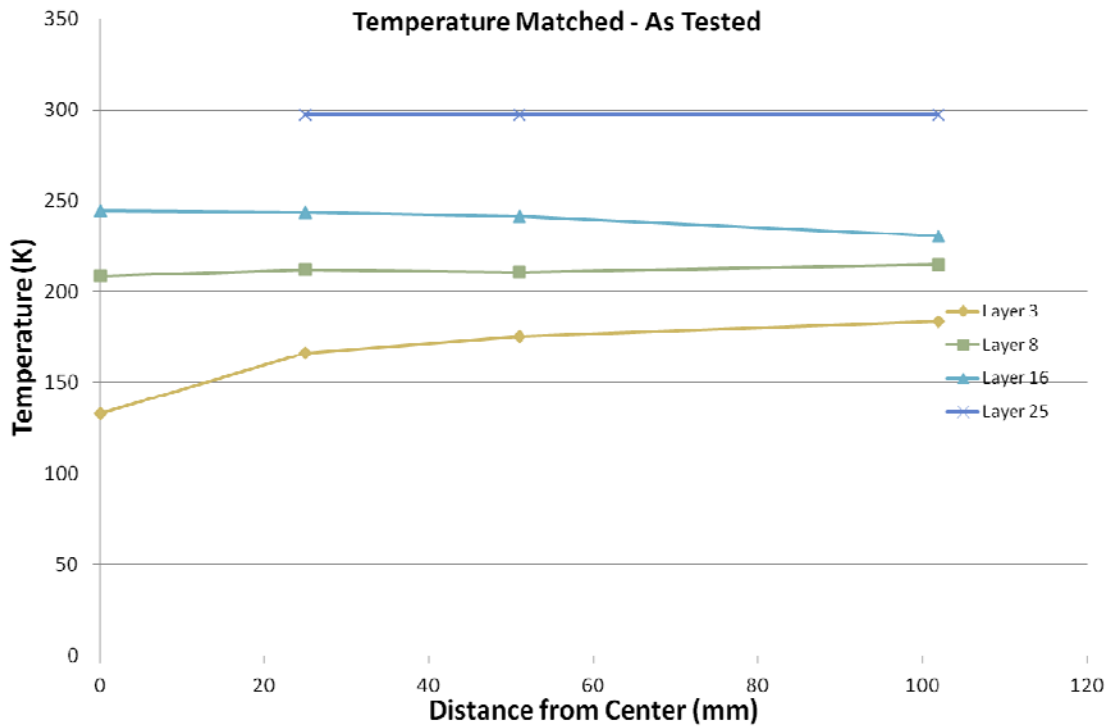
Cryostat-600: Temperature Profiles
P106, 1" Cryolite Buffer, 0.5" strut



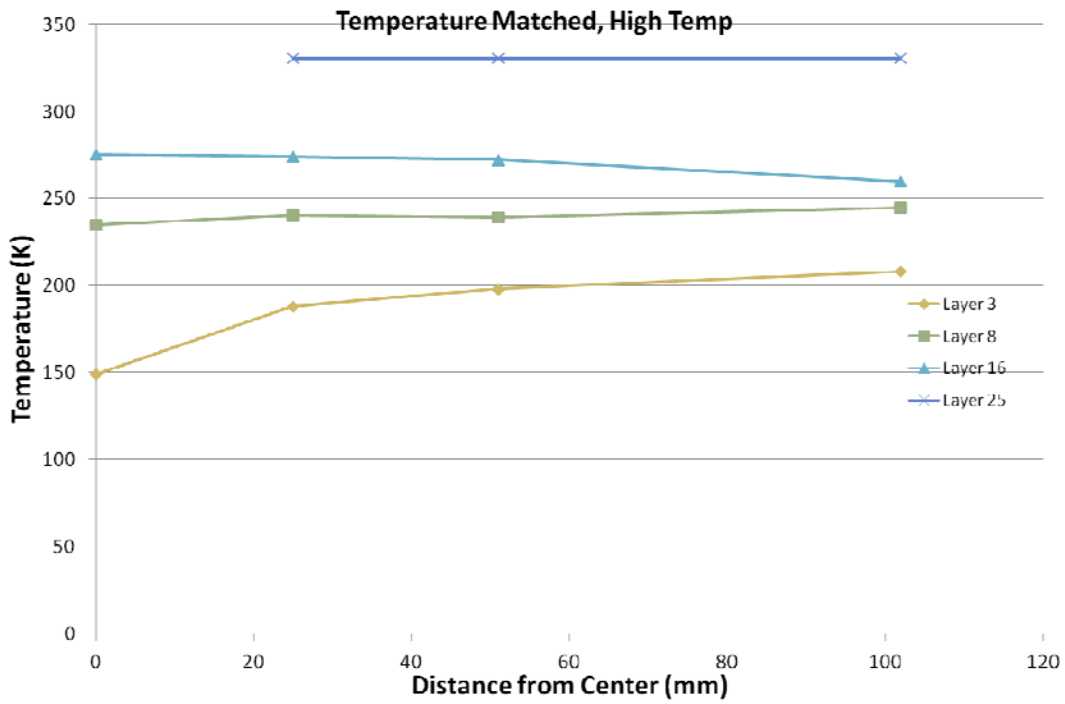
Cryostat-600: Temperature Profiles
P108, 1" Aerogel Bead Pack, 0.5" strut



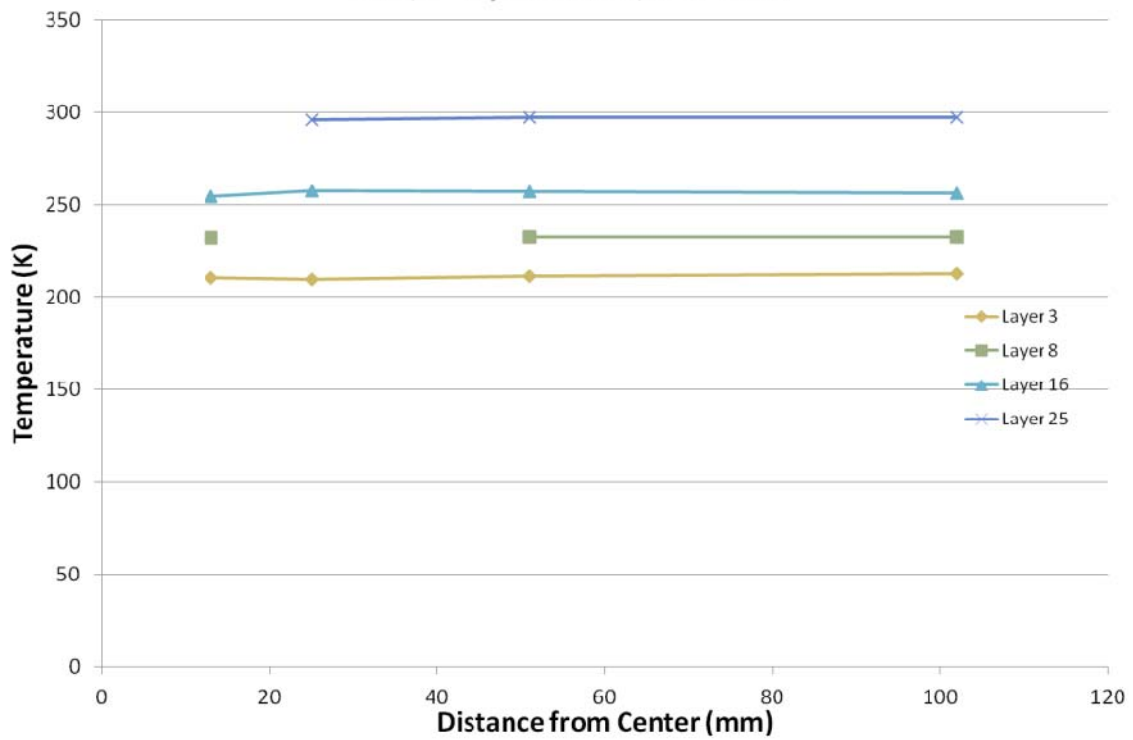
Cryostat-600: Temperature Profiles
P111, Test 1, 01/25/12
Temperature Matched - As Tested



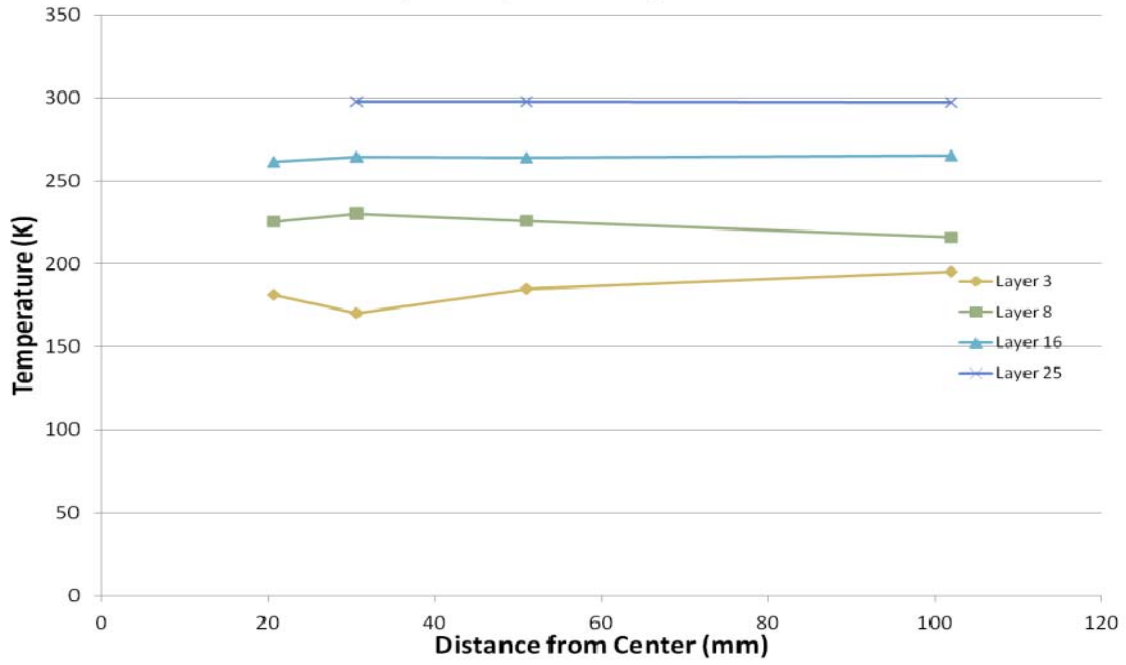
Cryostat-600: Temperature Profiles
P111, Test 2, 01/27/12



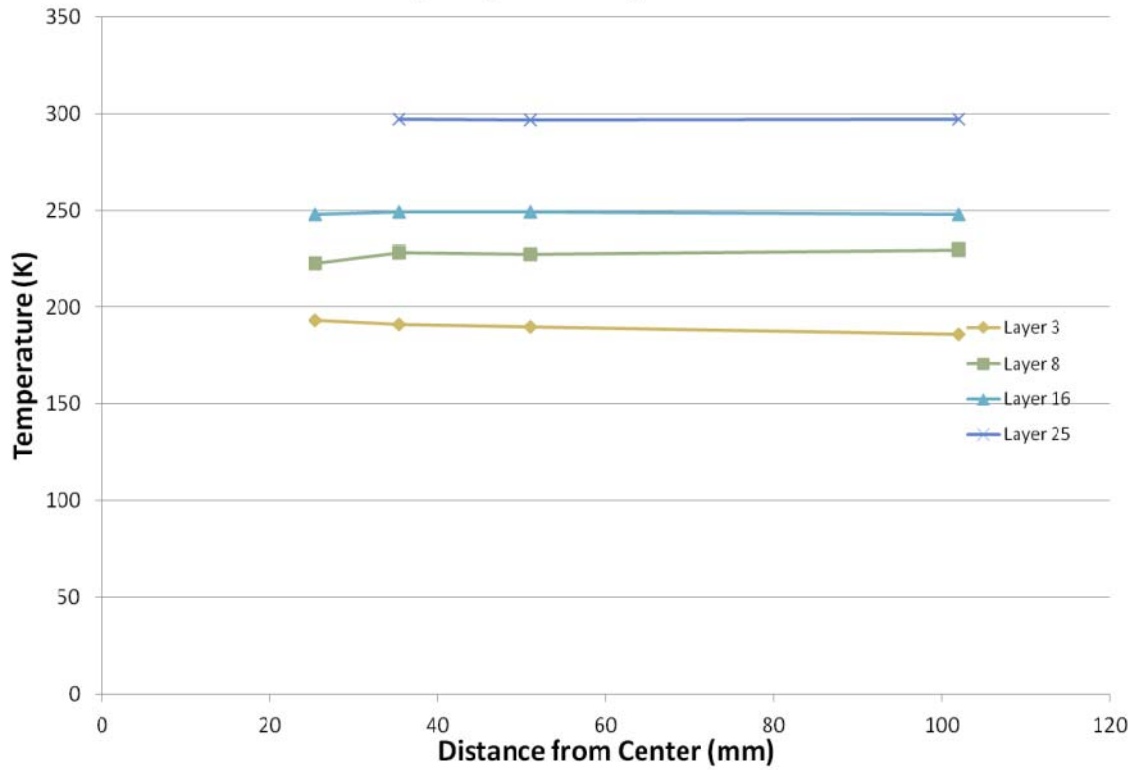
Cryostat-600: Temperature Profiles
P115, 1" Cryolite Buffer, 0.25" strut



Cryostat-600: Temperature Profiles
P117, 1.0" Cryolite buffer, 1.0" strut



Cryostat-600: Temperature Profiles
P121, Composite Strut, 1.0" buffer



Appendix B – Sample Calculation

Calculate the degradation due to a 104 mm (4 inch) pipe going through 60 layers of MLI using an 8 mm (~0.75 inch) Cryolite buffer. The system has a cold boundary temperature of 77 K and a warm boundary temperature of 297 K.

$$dq = q_{ref} \left(\frac{q_{actual}}{q_{ref}} \right)_{\#layers} \left(\frac{q_{ref}}{q_{ref}} \right)_{buffer\ thickness} \left(\frac{q_{actual}}{q_{ref}} \right)_{diameter} \left(\frac{q_{actual}}{q_{ref}} \right)_{buffer\ thickness} \left(\frac{T_h}{297} \right)^{.64}$$

For reference case one use 25 layers of MLI with a 76.2 mm penetration and a 6.4 mm Cryolite buffer.

Qref equals 0.052 W from

Figure 23.

For reference case two use 25 layers of MLI with a 76.2 mm penetration and a 12.7 mm Cryolite buffer. Qref' then equals 0.086 W from

Figure 24: Change in Heat Leak with Buffer Thickness

.

Q actual for the pipe diameter (using a 104 mm penetration with 25 layers of MLI & 6.4 mm Cryolite buffer) is 0.076 W from

Figure 23.

Q actual for the buffer thickness (using an 8 mm Cryolite buffer with 76.2 mm penetration and 25 layers) is 0.088 W from Figure 24.

Q actual for the number of layers (using 60 layers with a 12.7 mm buffer and a 76.2 mm penetration) is 0.038 W from

Figure 24: Change in Heat Leak with Buffer Thickness

Since the WBT is 297 K, we can neglect that term as 1

$$dq = 0.052 \left(\frac{0.038}{0.086} \right)_{\#layers} \left(\frac{0.086}{0.052} \right)_{buffer\ thickness} \left(\frac{0.076}{0.052} \right)_{diameter} \left(\frac{0.088}{0.052} \right)_{buffer\ thickness} = 0.095W$$

Appendix C – Uncertainty Analysis Derivations

The effect of a penetration on the heat leak thru MLI was not measured directly; it is calculated based on the measurements of other parameters during two tests. In the first test the heat leak through MLI without any penetration is measured once steady state conditions are reached, then a penetration is added and the heat leak again measured. The effect of the penetration on the steady state heat leak of the MLI can be calculated:

$$\Delta Q_{Pen} = Q_{meas} - Q_{MLI} - Q_{Strut}$$

Where,

- ΔQ_{Pen} – Change in heat leak of MLI due to penetration
- Q_{meas} – Total measured heat leak of MLI and penetration during the second test
- Q_{MLI} – Heat leak thru MLI only measured in the first test
- Q_{Strut} – Heat leak due to the penetration

The heat leak through the penetration, Q_{Strut} , is calculated from the temperature change over a section of the penetration outside of the MLI:

$$Q_{Strut} = \frac{k A (\Delta T)}{x}$$

Where,

- k – thermal conductivity of the strut material
- A – cross-sectional area of the strut in the area where ΔT is measured
- ΔT – change in temperature along the length of the strut
- x – distance between temperature measurements

The heat leak through the MLI, Q_{MLI} , is determined by measuring the rate of boiloff for liquid nitrogen:

$$Q_{MLI} = V \rho h_{fg}$$

Where,

- V – Volumetric flow rate of nitrogen
- ρ – Density of gaseous nitrogen
- h_{fg} – Heat of vaporization of nitrogen at atmospheric pressure

Q_{meas} is determined the same way during the penetration test. So the change in heat leak is:

$$\Delta Q_{pen} = f(k, A, \Delta T, x, V, \rho, h_{fg})$$

Each parameter contains an amount of uncertainty which combines to cause error in the final calculated thermal conductivity value. Returning to the definition of uncertainty above, the total uncertainty is:

$$U_{\Delta Q_{open}}^2 = \left(\frac{\delta \Delta Q_{pen}}{\delta Q_{strut}} \right)^2 U_{Q_{strut}}^2 + \left(\frac{\delta \Delta Q_{pen}}{\delta Q_{meas}} \right)^2 U_{Q_{meas}}^2 + \left(\frac{\delta \Delta Q_{pen}}{\delta Q_{MLI}} \right)^2 U_{Q_{MLI}}^2$$

$$U_{\Delta Q_{open}}^2 = U_{Q_{strut}}^2 + U_{Q_{meas}}^2 + U_{Q_{MLI}}^2$$

From the definition of Q_{strut} ,

$$U_{Q_{strut}}^2 = \left(\frac{\delta Q}{\delta k} \right)^2 U_k^2 + \left(\frac{\delta Q}{\delta A} \right)^2 U_A^2 + \left(\frac{\delta Q}{\delta \Delta T} \right)^2 U_{\Delta T}^2 + \left(\frac{\delta Q}{\delta x} \right)^2 U_x^2$$

The partial derivatives for these four variables are shown:

$$\frac{\delta Q}{\delta k} = \frac{A \Delta T}{x}$$

$$\frac{\delta Q}{\delta A} = \frac{k \Delta T}{x}$$

$$\frac{\delta Q}{\delta \Delta T} = \frac{k A}{x}$$

$$\frac{\delta Q}{\delta x} = -\frac{k A \Delta T}{x^2}$$

Substituting and simplifying results in,

$$U_{Q_{strut}}^2 = \left(\frac{k A \Delta T}{x} \right)^2 \left[\left(\frac{U_k}{k} \right)^2 + \left(\frac{U_A}{A} \right)^2 + \left(\frac{U_{\Delta T}}{\Delta T} \right)^2 + \left(\frac{U_x}{x} \right)^2 \right]$$

From the definition of Q_{MLI}

$$U_{Q_{MLI}}^2 = \left[\left(\frac{\delta Q}{\delta V} \right)^2 U_V^2 + \left(\frac{\delta Q}{\delta \rho} \right)^2 U_\rho^2 + \left(\frac{\delta Q}{\delta h_{f\bar{g}}} \right)^2 U_{h_{f\bar{g}}}^2 \right]_{Q_{MLI}}$$

The partial derivatives for these four variables are:

$$\frac{\delta Q}{\delta V} = \rho h_{f\bar{g}}$$

$$\frac{\delta Q}{\delta \rho} = V h_{f\bar{g}}$$

$$\frac{\delta Q}{\delta h_{f\bar{g}}} = V \rho$$

Substituting and simplifying:

$$U_{Q_{MLI}}^2 = \left[\left(\frac{\delta Q}{\delta V} \right)^2 U_V^2 + \left(\frac{\delta Q}{\delta \rho} \right)^2 U_\rho^2 + \left(\frac{\delta Q}{\delta h_{f\bar{g}}} \right)^2 U_{h_{f\bar{g}}}^2 \right]_{Q_{MLI}}$$

$$U_{Q_{MLI}}^2 = (\rho h_{f\bar{g}} V_{Q_{MLI}})^2 * \left[\left(\frac{U_V}{V} \right)^2 + \left(\frac{U_\rho}{\rho} \right)^2 + \left(\frac{U_{h_{f\bar{g}}}}{h_{f\bar{g}}} \right)^2 \right]_{Q_{MLI}}$$

And from the definition of Q_{meas}

$$U_{Q_{meas}}^2 = \left[\left(\frac{\delta Q}{\delta V} \right)^2 U_V^2 + \left(\frac{\delta Q}{\delta \rho} \right)^2 U_\rho^2 + \left(\frac{\delta Q}{\delta h_{f\bar{g}}} \right)^2 U_{h_{f\bar{g}}}^2 \right]_{Q_{meas}}$$

The Q_{meas} and Q_{MLI} uncertainty terms are the same. Substituting the partial derivatives results in:

$$\begin{aligned}
U_{\Delta Q_{open}}^2 &= \left(\frac{kA \Delta T}{x} \right)^2 \left[\left(\frac{U_k}{k} \right)^2 + \left(\frac{U_A}{A} \right)^2 + \left(\frac{U_{\Delta T}}{\Delta T} \right)^2 + \left(\frac{U_x}{x} \right)^2 \right] \\
&+ \left(\rho h_{fg} V_{Q_{MLI}} \right)^2 * \left[\left(\frac{U_V}{V} \right)^2 + \left(\frac{U_\rho}{\rho} \right)^2 + \left(\frac{U_{h_{fg}}}{h_{fg}} \right)^2 \right]_{Q_{MLI}} \\
&+ \left(\rho h_{fg} V_{Q_{meas}} \right)^2 * \left[\left(\frac{U_V}{V} \right)^2 + \left(\frac{U_\rho}{\rho} \right)^2 + \left(\frac{U_{h_{fg}}}{h_{fg}} \right)^2 \right]_{Q_{meas}}
\end{aligned}$$

(8)

The error terms in brackets for Q_{MLI} and Q_{meas} will be the same in the previous equation. The flowrates, however, will be different for each test:

$$\begin{aligned}
U_{\Delta Q_{open}}^2 &= \left(\frac{kA \Delta T}{x} \right)^2 \left[\left(\frac{U_k}{k} \right)^2 + \left(\frac{U_A}{A} \right)^2 + \left(\frac{U_{\Delta T}}{\Delta T} \right)^2 + \left(\frac{U_x}{x} \right)^2 \right] \\
&+ \left(\rho h_{fg} \right)^2 (V_{Q_{MLI}}^2 + V_{Q_{meas}}^2) * \left[\left(\frac{U_V}{V} \right)^2 + \left(\frac{U_\rho}{\rho} \right)^2 + \left(\frac{U_{h_{fg}}}{h_{fg}} \right)^2 \right] \\
U_{\Delta Q_{open}} &= \sqrt{\left(\frac{kA \Delta T}{x} \right)^2 \left[\left(\frac{U_k}{k} \right)^2 + \left(\frac{U_A}{A} \right)^2 + \left(\frac{U_{\Delta T}}{\Delta T} \right)^2 + \left(\frac{U_x}{x} \right)^2 \right] + \left(\rho h_{fg} \right)^2 (V_{Q_{MLI}}^2 + V_{Q_{meas}}^2) * \left[\left(\frac{U_V}{V} \right)^2 + \left(\frac{U_\rho}{\rho} \right)^2 + \left(\frac{U_{h_{fg}}}{h_{fg}} \right)^2 \right]}
\end{aligned}$$

And the percent error would be,

$$\frac{U_{\Delta Q_{open}}}{Q_{\Delta Q_{open}}} = \frac{\left\{ \left(\frac{kA \Delta T}{x} \right)^2 \left[\left(\frac{U_k}{k} \right)^2 + \left(\frac{U_A}{A} \right)^2 + \left(\frac{U_{\Delta T}}{\Delta T} \right)^2 + \left(\frac{U_x}{x} \right)^2 \right] + \left(\rho h_{fg} \right)^2 (V_{Q_{MLI}}^2 + V_{Q_{meas}}^2) * \left[\left(\frac{U_V}{V} \right)^2 + \left(\frac{U_\rho}{\rho} \right)^2 + \left(\frac{U_{h_{fg}}}{h_{fg}} \right)^2 \right] \right\}^{0.5}}{Q_{\Delta Q_{open}}}$$